SYNTHESIS AND CHARACTERIZATIONS OF ZnO AND ZnO/CNT NANOCOMPOSITES FOR APPLICATION IN SOLAR CELL

BY

ISAH, Haruna

MTech/SPS/2017/7093

DEPARTMENT OF PHYSICS

FEDERAL UNIVERSITY OF TECHNOLOGY MINNA

OCTOBER, 2021.

TITLE PAGE

SYNTHESIS AND CHARACTERIZATIONS OF ZnO AND ZnO/CNT NANOCOMPOSITES FOR APPLICATION IN SOLAR CELL

BY

ISAH, Haruna

MTech/SPS/2017/7093

A THESIS SUBMITTED TO THE POST GRADUATE SCHOOL FEDERAL UNIVERSITY OF TECHNOLOGY, MINNA, NIGERIA IN PARTIAL FULFILLMENT OF THE REQUIREMENTS FOR THE AWARD OF THE DEGREE OF MASTER OF TECHNOLOGY IN SOLID STATE PHYSICS

OCTOBER, 2021

ABSTRACT

Low power conversion efficiency resulting from recombination of photogenerated charges in TiO_2 based photovoltaic devices has caused serious challenges in photoelectrode efficiency of such devices. Hence the need to replace TiO_2 with ZnO and the composite of Zinc Oxide and Carbon Nanotube (ZnO/CNT) at optimised ratio to minimise the loss of photogenerated electrons during the photovoltaic activity is important. Hydrothermal synthesis was used to synthesis nanostructured ZnO and ZnO/CNT in the ratios of 0.1, 0.3 and 0.5 wt%. The synthesised nanostructured ZnO/CNT at different ratios were subjected to optical and structural characterisations using UV-Vis spectroscopy and X-ray diffraction spectroscopy (XRD). It was observed that the presence of CNTs enhanced the optical properties of ZnO with increasing concentration of the CNTs whilst the XRD data showed the presence of nanostructured crystalline phase of geometrical cubic and hexagonal planes of ZnO at (100), (002), (101), (110) and (102). The composite synthesised using hydrothermal synthesis revealed the suitability of the photo electrode to be used in solar cell application.

TABLE OF CONTENTS

LIST OF TABLES

Table **Page**

LIST OF FIGURES

CHAPTER ONE

1.0 INTRODUCTION

1.1 Background of the Study

During the last two decades, the global energy demands have rapidly increased and all predictions indicate that this growth will continue in both developed and developing nations (Mohammaznezhad *et al*., 2018). The effort to reduce energy crisis and global warming has given rise to high demand for highly performing solar energy conversion and energy storage devices (Chandu *et al*., 2017).

Different forms of fossil fuels including coal, oil and natural gas make up 80% of the world's energy use, yet they have major environmental impacts starting from climate change. In this scenario, the development of renewable energy sources, for instance solar energy, is crucial and urgent (Mohammaznezhad *et al*., 2018).

Photovoltaic energy conversion could solve energy problems, as it is reliable, renewable and sustainable globally. Solar energy is one of the cleanest energy resources, with the potential to replace a significant percentage of fossil fuels use due to its availability and abundance. Solar energy can be converted into thermal or electrical energy, or into a liquid fuel like hydrogen (Chandu *et al*., 2017).

Solar energy is the most abundant source of energy on Earth which is pouring on our planet. The rate at which it is received every minute, suffices to cover the world's energy demand for a year (Dey *et al*., 2016). Of all the energy produced, on a daily bases today, solar energy constitute about 1% while substantial fraction comes from the use of non-renewable energy sources which are not sustainable, environmental unfriendly and could even endanger the mere existence of life on Earth (Lee *et al*., 2015).

To convert solar energy to benefit humanity, suitable devices for such work are required. These devices are called photovoltaic devices. A photovoltaic device must have good photocatalytic capability in order to serve the purpose (Septiani *et al*., 2017).

Over the past decades, there is an enormous advancement in new materials along with their technological applications in various fields. Semiconducting metal oxide nanomaterials like: ZnO, SnO_2, Fe_2O_3 & TiO_2 have emerged as optimistic UV sensitive materials with applications in various optoelectronic devices (Lai *et al*., 2013). Among them, ZnO is one of the most researched transparent conductive oxides (TCOs). ZnO has wide energy gap of 3.37 eV and large binding energy of exciton of 60 meV. It is biocompatible, highly photostable and is used for the assemblage of blue LEDs and lasers. ZnO is an economically viable TCO to cover the UV spectral band ranging from 240 to 380 nm and is transparent to the visible light (Shkir *et al*., 2020).

Zinc oxide (ZnO) has received great attention in several fields of application due to its sensitivity to environmental factors such as humidity, gas species and light irradiation. Indeed, such factors can determine physico-chemical changes of ZnO that can be suitably used in photocatalytic apllications (Lee *et al*., 2016; Mei *et al*., 2018).

The morphology of ZnO is very interesting due to the rich nanostructures obtained under different methods and synthesis conditions. Hence, these nanostructures offer large potential to be applied in a wide range nanoscale devices (Luo *et al*., 2016). Along with this, carbon nanotubes (CNTs) were reported as a strong material, even stronger than steel and at the same time, CNTs are really light. Other than that, CNTs display extraordinary electrical, thermal and chemical properties which gives many advantages in optoelectronic devices (Septiani *et al*., 2017).

On the other hand, the favourable optoelectronic properties of carbon nanotubes (CNTs) have attracted more research interest for photonic applications. CNTs are known for their high electrical conduction, carrier mobility and a wide optical transmittance which can be tunable by the process of doping with other metal oxide materials like ZnO (Xolani *et al*., 2017).

1.2 Statement of the Research Problem

Photoelectrode in DSSCs made from TiO_2 nanoparticles (NPs) films coated onto fluorine-doped tin oxide (FTO) is suitable for its chemical affinity, large surface area for dye adsorption and high energy band gap for good charge transfer between the electrolytes and dye (Fang *et al*., 2015).

However, the persistent problem of DSSCs is that not all of the photo-generated electrons can arrive at the collecting electrode, because electron transport within the photo-anode nanoparticle film of TiO_2 network takes place via a series of jumps to adjacent particles, and the energy damage that occurs during charge transport processes results in reduced power conversion efficiency (PCE) of the DSSC (Fang *et al*., 2015). However, researchers have tried to solve the recombination problem in TiO_2 based DSSCs by increasing the size of the photoanode film thickness but it rather consequently resulted in aggravating the problem by extending the distance which the electrons diffuse through to the TCO collector. In view of this, it is proposed in this study to replace TiO_2 with ZnO because unlike TiO_2, the life span of electrons in ZnO is generally extended with minimised recombination losses especially if nanostructured ZnO is hydrothermally synthesised (Laurent *et al*., 2015). This is because electrons can easily be led through a direct path within nanostructures of ZnO rather than by multiple-scattering transport between nanoparticles in TiO_2.The electron transport is tens to hundreds of times faster in ZnO based DSSCs than in TiO_2 based DSSCs.

Introducing CNTs into the ZnO lattices initiates modification in the density of outermost orbital state and the Fermi level. This causes an enhancement of photo activity of the material thereby increasing its transparency to visible light and conductivity. This consequently addresses the problem of dye anchorage on ZnO film when used as photoanode film in DSSCs. When 1D ZnO nanostructures are hydrothermally synthesised, doped with CNTs, and its ZnO/CNT composite used for photoanode in DSSC, the surface activity of the composite film is greatly enhanced and it in turn boosts the PCE of the DSSC (Deepti *et al.*, 2017).

1.3 Aim and Objectives of the Study

The aim of this study is to hydrothermally synthesise ZnO and use ZnO/CNT nanocomposites for photoanode in photovoltaic devices.

The objectives of the study is to:

1. synthesise nanostructured ZnO using hydrothermal synthesis.
2. fabricate the photoelectrodes of ZnO and ZnO/CNTs composites.
3. characterise the prepared samples using x-ray diffraction spectroscopy (XRD) and ultraviolet-visible spectroscopy (UV-Vis).

1.4 Significance of the Study

Combining the bio-safety and environmental friendliness of ZnO with the simplicity and affordability of its synthesis has pave way for entrepreneurial opportunities in production of cosmetics in our immediate environment. The conversion from solar energy to electricity is fulfilled by photovaltaic devices based on the photovoltaic effect. Many photovoltaic devices have already been developed over the past few decades. However, conversion efficiency and cost are the drawbacks limiting its wide-spread use. ZnO photoelectrode can be used in photovoltaic devices, especially when enhanced with CNT, to solve the conversion efficiency problem. The results acquired from this study will also provide additional knowledge for manufacturing photovoltaic devices through the use of cost-effective methods such as hydrothermal method.

1.5 Scope and Limitation of the Study

1.5.1 Scope of the Study

This study considered the synthesis of nanostructured ZnO using hydrothermal synthesis. The study also covered the enhancement of the as-synthesized ZnO with CNTs using direct mixing method of doping. Furthermore, the study also included the fabrication of ZnO and ZnO/CNT photoanodes with 0.1 wt%, 0.3 wt% and 0.5 wt% concentrations of CNT. The fabricated photoanodes were as well characterised using XRD and UV-Visible Spectroscopy.

1.5.2 Limitation of the Study

Scanning Electron Microscopy/Energy Dispersive Spectroscopy (SEM/EDS) was carried out twice at different laboratories but the magnification of the images were poor hence SEM/EDS not presented in here.

CHAPTER TWO

2.0 LITERATURE REVIEW

2.1 Nanomaterials and their Applications

It is notable that nanostructured materials have properties that are characterized by sizes that are smaller than 100 nm. As a wide scope, for example, electrical conductivity property, relies upon nanometer-scale, the term "nanostructured material" can incorporate generally, many materials (Whitesides *et al*., 2002). A motivation behind why this class of materials is viewed as especially fascinating is the advantage to obtain "materials-by-structure" (Bréchignac *et al*., 2008).

There are commonly two methodologies for fabricating nanostructures. These are the "top-down" and "bottom-up" methods. The "top-down" procedure can be understood as the development of nanoscale structures by evacuating or subtracting portions of a bulk material. The "bottom-up" strategy includes the gathering of sub nanoscale structures (materials) to construct the required nanostructure (Hoshino *et al*., 2004). The "bottom-up" technique has the advantage of having the option to manufacture very fine structures (Demianets *et al*., 2002).Nanostructured materials can be grouped into three (3) unique families: grouping by size, function and structures as shown in the table below.

Table 2.1: Arrangement of nanostructures into three different groups with each group identifying some parameters.

S/N	Size	Function	Structure
1	Molecular (1-6 nm)	Electronic	Surface and interfaces
2	Colloidal (1-100 nm)	Optical	Mechanical properties
3	Micro/Nanofabricated (70-100 nm)	Magnetic	

Nanostructures have found applications in different areas including the generation of electronic parts, sensors, multifunctional materials, organized colloids. They can likewise be utilized inside assembling forms and the control of surface.

2.2 Carbon Nanotubes (CNTs)

Carbon nanotubes (CNTs) have been a star material for many years resulting from its interesting structure and many outstanding properties. CNTs are made of hexagonal structure with alternative single and double bonds. They have superior physical properties, such as high mechanical strength, high specific surface area, high transparency in the visible range, high electrical conductivity and high thermal conductivity (Laird *et al*., 2015). They have found important application in many areas including composites, transparent electrode, charge-transport buffer layer and electrocatalysts (Lu *et al*., 2015).

2.2.1 Classification of CNTs

CNTs in terms of the number of the graphene sheets can be classified into:

i. Single-walled (SWCNTs) and
ii. Multiwalled (MWCNTs).

A SWCNT can be considered as a seamless cylinder formed by the rolling up of a graphene sheet along the hexagonal crystal lattice of grapheme. The bandgap of a semiconductive SWCNT is inversely proportional to its diameter.

MWCNTs can be considered as a cylinder formed by the rolling up of two or more graphene sheets. MWCNTs are always metallic (Losurdo *et al*., 2011).

SWCNTs and MWCNTs can be fabricated by a couple of techniques such as chemical vapour deposition (CVD), laser ablation, arc discharge and high-pressure carbon monoxide disproportionation (HiPCO) (Zheng *et al.*, 2012).

CNTs have interesting extraordinary properties. The electron transport in a SWCNT has ballistic behaviour. Thus, they can have high charge carrier mobility. For example, the charge carrier mobility of CNT is about 20000 $cm^2 \cdot V^{-1} \cdot s^{-1}$ (Hao *et al.*, 2018). They also have excellent thermal conductivity. The thermal conductivity of CNT is 3000 W/mK to 5000 W/mK (Li *et al.*, 2018). In addition, they have high transmittance in the visible range. Thus, they can be used as the transparent electrode of optoelectronic devices such as solar cells. Their good conductivity together with high surface area also leads to their important application as catalyst support. They can be even directly used as electrocatalysts for chemical reactions (Gao and Duan, 2015).

2.3 ZnO Crystal Structure

The ZnO crystal is hexagonal wurtzite and exhibits partial polar characteristics (Gratzel, 2005) with lattice parameters a = 0.3296 and c = 0.52065 nm (Wang, 2004). The structure of ZnO can be described as a number of alternating planes composed of tetrahedrally coordinated O^{2-} and Zn^{2+} stacked alternately along the c-axis. The tetrahedral coordination in the metal oxide takes into account a non-focal symmetric structure, hence prompts both piezoelectric and pyroelectric properties (Yogamalar and Bose, 2013).

There are three structures of ZnO crystal that commonly exist; hexagonal wurtzite, cubic zinc blende and a cubic rock salt (Sodium Chloride type) structure. The hexagonal wurtzite structure is the most widely recognized, the zinc-blende structure is metal stable and can be developed only on cubic structures (Cauda *et al.*, 2014). A cubic rock-salt structure must be balanced out under extreme pressures (Moezzi *et al.*, 2012).

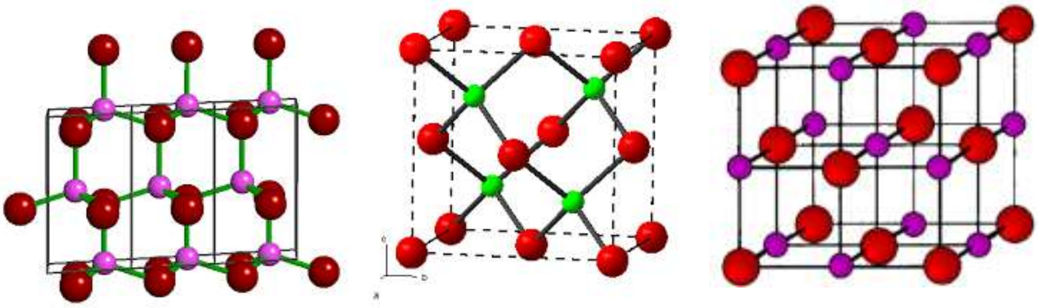

(a) Hexagonal wurtzite (b) Cubic zinc blende (c) Cubic rock salt

Figure 2.1: Representation of ZnO crystal structures. The small and big spheres denote zinc and oxygen atoms respectively.

Akermi *et al*. (2013) the wurzite structure is hexagonal cross section consisting noncentrosymmetric symmetry and polar surfaces as shown in Figure 2.1. The structure has a place with the space group P63mc and is described by two interconnecting sublattices of Zn^{2+} and O^{2-}, to such an extent that each zinc ion is encompassed by a tetrahedral of oxygen ions, and the other way around (Jagadish and Pearton, 2011).

The most common polar surface is the basal plane (001) (Wang, 2004). One end of the basal polar plane terminates with partially positive Zn lattice sites and the other end terminates in partially negative oxygen lattice sites (Saito *et al*., 2002). The oppositely charged ions produce positively charged Zn-(0001) and negatively charged O-(0001) surfaces, resulting in a normal dipole moment and spontaneous polarization along the c-axis as well as a variance in surface energy (Emanetoglu *et al*., 2009). To maintain a stable structure, the polar surfaces generally have facets or exhibit massive surface reconstructions, but ZnO± (0001) surfaces are exceptions: they are atomically flat, stable and exhibit no reconstruction (Chen *et al*., 2000). Efforts to understand the superior stability of the ZnO± (0001) polar surfaces are at the forefront of research in today's surface physics (Liang *et al*., 2011). ZnO generally known as n-type semiconductor is a material with high bond energy of 60meV (Kumaresan *et al*., 2016). It has high thermal and mechanical stability at room temperature (Agnieszka and Teofil, 2014), conduction band edge found to be very close to that of TiO_2 (ca-4.4eV) (Laurent *et al*., 2015), and wide band gap energies of 3.37eV and 3.34eV at room temperature and low temperature respectively (Akhiruddin *et al.*, 2014).

ZnO has lattice parameters a=3.249Å and c=5.206Å and a hexagonal (wurtzite) crystal structure (Akhiruddin *et al.*, 2014). These all put together, gives ZnO a unique electronic, optical (Xiaobin *et al.*, 2012), physical and chemical properties rooting its application in photonics (Sunandan and Joydeep, 2009), electronics, optoelectronics and laser technology (Arya *et al.*, 2012), and hydrogen production (Kumaresan *et al.*, 2016). The hardness, rigidity and piezoelectric constant of ZnO pave way for its high placement in ceramics industry while its application in biomedical and pro-ecological systems results from its less toxic nature, biocompatible and biodegradable hallmarks (Agnieszka and Teofil 2014). Applications in DSSCs, polymer-inorganic hybrid solar cells (PIHSCs), piezoelectric nanogenerators (Xiaobin*et al.*, 2012), pharmaceuticals to use as a coating additive (Look, 2001), acoustic wave filters, photonic crystals, photo detectors, light emitting diodes, photodiodes, optical modulator waveguides, solar cells and varistors (Sunandan and Joydeep, 2009), gas sensors, UV light sensors, photo catalysts, thin film transistors (TFTs), transparent conducting layers, light emitting devices, and as blocking layer in flexible organic solar cell have so far been identified with ZnO (Akhiruddin *et al.*, 2014).

ZnO thin films has been synthesised since 1960s where it was applied in sensors, transducers and as photocatalysts. In recent times, study of one-dimensional (1D) material has gained important value in nanoscience and nanotechnology (Sunandan and Joydeep, 2009). Edelstein and Cammaratra (1998) reported that nanomaterials are now an established research field over many different scientific and engineering disciplines and are interesting systems for basic scientific investigations as well as for application within current technologies. Novel electrical, chemical, mechanical and optical properties accompany the surface and quantum confinement effects of a material as its particle size decreases (Haruna *et al.*, 2019).

A well-known versatile way to engineer the electrical and optical properties of ZnO nanostructures (NSs) is by metal doping. Introducing metal into the ZnO lattices initiates modification in the density of outermost orbital state and the Fermi level. This causes an enhancement of photo activity of the material (Iwantono *et al*., 2016). An attractive method to enhance the photocatalytic and structural activities of ZnO is to couple it with carbon materials such as, activated carbon, graphene, carbon nanotubes (CNTs) and graphite oxide (Deepti *et al*., 2017). Doping ZnO with carbon nanotubes can increase its conductivity and transparency to visible light (Sunandan and Joydeep, 2009).

Prayut *et al*. (2010) have reported that CNTs have also drawn much attention since they were discovered because of their unique fundamental structure and physical properties; one dimensional (1D) structure and large surface area, distinguished mechanical and electronic properties, leading to potential high-technology applications. In addition, CNT provides a strong Vander Waals bonding and various well-defined adsorption sites available to the adsorbing molecules. It is believed that novel functionality will exist when the extraordinary properties of ZnO are combined with that of CNTs, especially when low dimensional (1D) composites are formed.

2.4 Applications of ZnO

ZnO is used in a wide scope of industrial applications as both a bulk material and a nanomaterial. ZnO is an attractive semiconductor due to its incredible properties that make it a suitable candidate in photoelectrochemical solar cells, electronics, ceramics, concrets, rubber/plastics, pharmaceuticals, oil and gas (Eman *et al*., 2016).

2.4.1 Solar cells and photocatalytic effects

The trapping process (energy damage during charge transport) in TiO_2 DSSC results in the transport becoming slow and an increase in scattering, which greatly increases the recombination of the electrons with the oxidised dye molecules. The need for an alternative to counteract the electron transport problems involved in DSSCs of TiO_2-based, propels the necessity to replace the semiconductor material (TiO_2) with a one-dimension nanostructured semiconducting metal oxide material (Fang *et al*., 2015).

Among the semiconducting metal oxide materials, ZnO is extensively studied due to its unique physicochemical, piezoelectric, optical and catalytic properties (Kumaresan *et al*., 2016). These properties are correlated with shape, size and morphology (nanostructures) of ZnO nanoparticles. Research has demonstrated that the electron transport is tens to hundreds of times slower in nanoparticle DSSCs than in nanostructure DSSCs (Fang *et al*., 2015). ZnO can be considered for the replacement of TiO_2 because in ZnO, the electrons can be transported smoothly spending a minimum time possible when its nanostructures are suitably and carefully grown (Laurent *et al*., 2015). A comfortable way to make better, the electron transport in DSSCs, is to replace the nanoparticle photoelectrode with a 1D nanostructured photoelectrode having nanostructures such as nanorods, nanosheets, nanaobelts (Fang*et al*., 2015), nano-needles, nano-helices, nano-springs, nano-ribbons, nano-tubes and nano-combs (Agnieszka *et al*., 2014), and nanowires, nanocombs, nanorings, nanobows, nanobelts (Sunandan *et al*., 2009). With regard to this, ZnO is expected to exhibit faster electron transport and reduced recombination damage as compared with TiO_2. Figures 2.2, 2.3 and 2.4 show the microscopic images distinguishing the nanostructured ZnO from the nanoparticle ZnO.

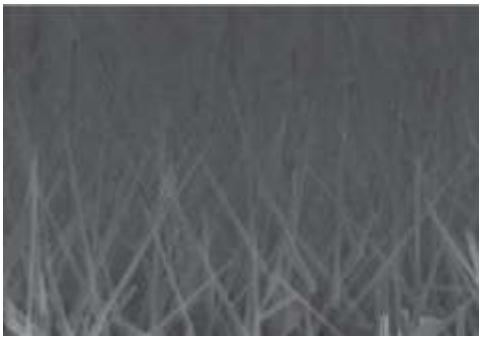

Figure 2.2: Scanning electron microscope (SEM) image of nanostructured ZnO nanowires (Chang and Lin, 2014)

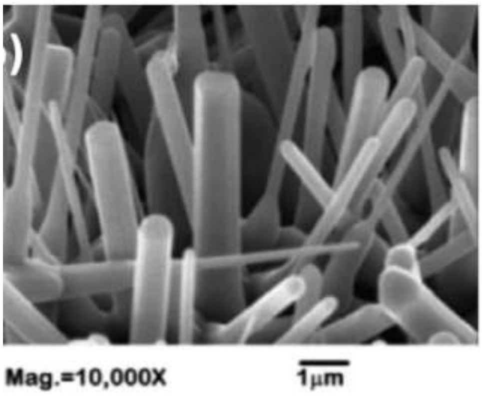

Figure 2.3: SEM image of nanostructured ZnO nanorods (Ong *et al*., 2018).

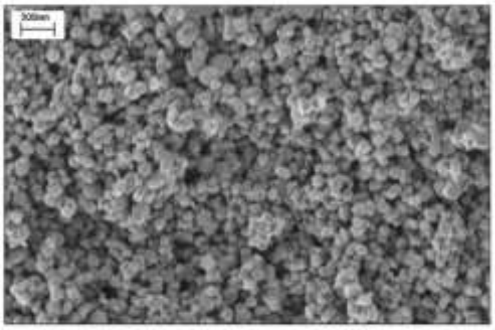

Figure 2.4: SEM image of ZnO-nanoparticles (Zhang *et al*., 2009).

However, studies have shown that the entire efficiency of TiO_2-based DSSCs is higher than that of ZnO-based DSSCs consequently resulting from the problem of dye absorption process in ZnO DSSCs. Since dyes have high carboxylic acid binding groups, ZnO dissolution and precipitation of dye-Zn^{2+} complexes occurs leading to a poor overall electron efficiency of the dye (Fang *et al*., 2015).

Incorporation of metal oxides with CNTs will lead to the formation of nanocomposites having the properties of both components which would be useful for photoelectrochemical (PEC) and photocatalytic activities as CNTs are very good electron acceptor (Deepti *et al*., 2017). The dye adsorption problem in ZnO is proposed to be solved by doping the ZnO with CNTs. CNTs enhances the surface activity of ZnO by widening its surface area and modifying its crystal structure, hence making available the room for good dye anchorage.

ZnO-based DSSC technology as alternative to TiO_2 is considered as one of the most promising materials for solar cells due to a faster electron transport with reduced recombination loss and its ease of crystallization and anisotropic growth (Zhang *et al*., 2012). It in this light that researchers like:

Sudhagar *et al*. (2011) reported jacks-like ZnO nanorod architecture as a photoanode in dye-sensitized solar cells and the result exhibited a higher conversion efficiency of $\eta = 1.82\%$ (V_{oc}= 0.59 V, J_{sc}= 5.52 mA cm^{-2}) than that of the branch-free ZnO nanorods electrodes ($\eta = 1.08\%$, V_{oc}= 0.49 V, J_{sc}= 4.02 mA cm^{-2}).

Cheng *et al*. (2008) fabricated ZnO nanowires and branched ZnO nanowires on conductive glass substrates via a solvothermal method for dye sensitized solar cells. The short-circuit current density 4.27 mA/cm^2 and the energy conversion efficiency 1.51%of the branched ZnO nanowire DSSCs when compared with those of ZnO nanowires, were higher than those of the bare ZnO nanowire.

Lupan *et al*. (2010) studied the well-aligned arrays of vertically oriented ZnO nanowires electrodeposited on indium doped tin oxide (ITO) coated glass for dye-sensitized solar cells. The maximum overall photovoltaic conversion efficiency was 0.66% at100 mW/cm^2.

Ko*et al*. (2011) compared different fabricated ZnO nanowire DSSCs that included lengthwise growth and branched growth. They showed that the overall light-conversion efficiency of the branched ZnO nanowire DSSCs was much higher than the upstanding ZnO nanowires. Owing this improvement to the enhanced surface area resulting in higher dye loading and light harvesting, and the reduction of charge recombination by providing direct conduction pathways along the crystalline ZnO "nanotree" multigeneration branches.

2.4.2 Electronics

In electronics, ZnO is used as varistors, piezoelectric transducers, sensors, surface acoustic wave devices, (Yogamalar and Bose, 2013), light emitting devices, memory devices, transparent transistors (Djurisic *et al*., 2012), gas sensors and photo-detectors (Eman *et al*., 2016).

2.4.3 Ceramics

In ceramics, ZnO serves as additive to improve heat capacity, thermal conductivity and high temperature stability of ceramic (tiles), and allows the development of different types and properties of surface finishing (reduces elasticity in the glaze to reduce cracking and shivering).

2.4.4 Concretes

In concrete, ZnO provides a longer processing time and improves the concretes resistance against water (Xia *et al*., 2003).

2.4.5 Rubber/plastics Production

ZnO is also used as an effect activator of the curing process of natural rubber to increase heat conductivity in tires, reduce devulcanization of rubber types and stabilization of latex foam. It is also used in plastics as an additive to tune properties such as viscosity, fire-resistance, and tensile strength, and as source of micronutrient zinc in agriculture. ZnO is a good colour additive to providing sacrificial cathodic protection within coatings (Yogamalar and Bose, 2013).

2.4.6 Pharmaceuticals

It is used in pharmaceutical as antiseptic healing creams and sun block lotions exhibiting antibacterial properties (Djurisic *et al.*, 2012).

2.4.7 Oil and Gas Companies

In oil and gas, ZnO is used as a bulk absorbent for the control of H_2S in drilling fluid formed by the presence of sulphate reducing bacteria (Yogamalar and Bose, 2013). It is also used as one of the mixed oxides in catalysts for the production of methanol and as a catalyst for the synthesis of *iso*butyl alcohol, formose sugars and the conversion of cyclohexanol to cylcohexane in the course of the production of caprolactam (a precursor for nylon) (Xia *et al.*, 2003).

2.5 Synthesis of ZnO

The basic techniques used for the synthesis of ZnO are broadly divided into:

i. physical methods
ii. biological methods and
iii. chemical methods (Ayesha *et al.*, 2017).

The physical methods are also called gaseous phase method (Sheng *et al.*, 2014). This method of synthesis involves the use of physical forces in the attraction of nanoscale particles to form large, stable and suitably-defined nanostructures (Happy *et al.*, 2017). In this method of synthesis, gaseous environment in closed chambers with high temperatures from 500˚C to 1500˚C is used to carry out the synthesis. Its examples include high energy ball milling, laser ablation, electro spraying, inert gas condensation (such as resistive evaporation, laser evaporation and sputtering), chemical vapor condensation, physical vapour deposition (PVD) (such as sputtering, electron beam evaporation, pulsed laser deposition; a physical vapour deposition technique where a high-power pulsed laser beam is focused inside a vacuum chamber to strike a target of the material that is to be deposited (Lawrence *et al*., 2013), and vacuumarc), laser pyrolysis, melt mixing. However, these methods are expensive and complicated (Sunandan and Joydeep, 2009).

Biosynthesis of NPs is an approach of synthesis which uses microorganisms and plants for the formation of ZnO NPs. This approach is an environment-friendly, cost- effective, biocompatible, safe, green approach (Abdul *et al*., 2014). Green synthesis can be carried out through plants, bacteria, fungi, algae etc. They allow large scale production of ZnO NPs free of additional impurities (Yuvakkumar *et al*., 2014).

The chemical (also called solution phase) method is done in aqueous solution with growth temperatures less than the boiling point of the aqueous solution which makes it simple with tolerable growth conditions (Sunandan and Joydeep, 2009). Chemical reactions in aqueous systems are usually considered to be in a reversible equilibrium, and the driving force is the minimization of the free energy of the entire reaction system, which is the intrinsic nature of wet chemical methods (Yangyang *et al*., 2012). Among chemical methods are sol-gel method (a chemical solution process used to make ceramic and glass materials in the form of thin film, fibres or powder), micro emulsion technique, co-precipitation method, hydrothermal synthesis, polyol synthesis, microwave assisted synthesis, chemical vapour synthesis, metal organic chemical vapour deposition (MOCVD) and plasma enhanced vapour deposition technique.

2.6 Hydrothermal Synthesis

Hydrothermal synthesis is a synthesis method of crystals that depends on the solubility of minerals in hot water under high pressure (Hiromichi and Yukiya, 2010). Hydrothermal synthesis usually refers to heterogeneous reactions in aqueous media above 100 ^{o}C under pressure. This is normally achieved by the use of an autoclave (a closed high-pressure growth vessel).

Hydrothermal method unlike other methods has the following advantages over other methods. Use of simple equipment, less expensive and requires little or/no effort; synthesis can be carried out without catalyst. It yields as-grown particles with, generally wide area and uniform distribution (Aleksandra *et al*., 2007). It is environmental friendly, does not require the use of natural solvents or extra handling of the product (crushing and calcinations) and completes synthesis at low temperatures without the use of complex vacuum setup (Tyona *et al*., 2013). Resulting shapes and dimensions of the as-synthesised crystals greatly rely upon the precursors, reaction temperature and pressure. Hydrothermal method can be used for production of stand-free nanostructures and obtain exact control of the nanostructure size desired (Aleksandra *et al*., 2007).The hydrothermal synthesis is capable of directly precipitating thin film coatings onto the surface of the substrate at low temperatures.

The hydrothermal method has gotten consideration lately as it aids synthesis of particles with desired properties (Jezequel *et al*., 2010). This can be achieved by controlling the basic factors of synthesis such as solution pH, reaction time and temperature, precursors, consideration of additives or templates and the type of solvent used (Sunandan *et al*., 2009).

2.6.1 Hydrothermal Synthesis of ZnO

Generally speaking, ZnO is expected to crystallize by the hydrolysis of Zn salts in a basic solution that can be formed using strong or weak alkalis (Sheng and Zhong 2008). Reports of hydrothermal synthesis in aqueous medium are available in the literature.

Baruwati *et al*. (2006) reported that ZnO nanoparticles were synthesized using zinc nitrate hexahydrate in aqueous solution where autoclave was used at a temperature of 120 ^{o}C with pH adjusted to 7.5 using ammonium hydroxide. The particles were dried at 80^{o}C after washing. The results shown in the transmission electron microscope (TEM) image revealed that the as-synthesized particles were having an average size of 50 nm.

Lu and Yeh (2000) have synthesised ZnO crystalline powder through hydrothermal process using $Zn(NO_3)_2$ and ammonia. The synthesis was carried out at 100^{o}C, 150^{o}C and 200^{o}C for 2h and the effect of growth temperature and pH were studied. The particle size of the ZnO powder synthesised varied from 0.7 µm to 0.9 µm, 1.3 µm and 1.5 µm as pH was increased from 9 to 10, 11 and 12.

Jiaguo *et al*. (2008) reported ZnO hollow spheres fabricated by a hydrothermal approach using $ZnCl_2$ as a zinc source and glucose as a basic source. The molar ratios of glucose to $ZnCl_2$ were varied from 0 to 20. The pH was adjusted to 5.5 and heated in an autoclave at 180 °C for 24 h. The results indicated that the average crystallite size, shell thickness, specific surface areas, pore structures, and photocatalytic activity of ZnO hollow spheres could be controlled by varying the molar ratio of glucose to $ZnCl_2$. With increasing glucose, the photocatalytic activity increases and reaches a maximum value at15.

Brintha and Ajitha (2015) synthesised ZnO nanoparticles method using zinc acetate and methanol as precursors. The mixture was heated at 100^{0}C for 6 h under autogenous pressure in an autoclave. Scanning Electron Microscopic investigation reveals that the surface morphology of ZnO nanoparticle is spherical with the average crystallite size of the nanoparticles observed to be 14 nm.

Karuna *et al*. (2018) prepared ZnO nanostructures with numerous morphology using hydrothermal method. $Zn(CH_3COO)_2{\cdot}2H_2O$ and NaOH were used as reagents in an aqueous solution. The synthesis was carried out in an autoclave at a temperature of 200 ^{o}C for 24 h after adjusting pH from 8 to10, 11 and 12. The final product was dried at 80 ^{o}C for 6 h. A high resolution SEM attached with an energy-dispersive X-ray analyzer (EDXA) was used to observe the morphology of synthesized ZnO and to determine the elemental compositions. Crystallite size of the as-synthesised ZnO varied from 15 nm, to 14.6 nm, 10.2 nm and 9.1nm as the pH was changed from 8 to10, 11 and 12 respectively. EDXA result confirms that ZnO powder contains only Zn and O elements. The average atomic percentage of Zn:O was 43.11:56.89 which shows that product was in nearly statiometric ratio.

An alkaline solution is essential for the formation of ZnO nanostructures because normally divalent metal ions do not hydrolyze in acidic environments. Generally speaking, the solubility of ZnO in an alkali solution increases with the alkali concentration and temperature. The commonly used alkali compounds are KOH and NaOH (Sheng *et al*., 2008). KOH is thought to be preferable to NaOH, because K^+ has a larger ion radius and thus a lower probability of incorporation into the ZnO lattice (Demianets *et al*., 2002). Furthermore, it has been suggested that Na^+ is attracted by the OH^- around the nanocrystal and forms a virtual capping layer, thus, inhibiting the nanocrystal growth. However, ZnO synthesised using NaOH always yield good dye impregnation than when KOH is used (Viswanatha *et al*., 2009).The main reactions involved in the growth are illustrated in the equations below (Sheng *et al*., 2008).

$$Zn^{2+} + 2OH^- \longleftrightarrow Zn(OH)_2 \qquad (2.1)$$

$$Zn(OH)_2 + 2OH^- \longleftrightarrow [Zn(OH)_4]^{2-} \qquad (2.2)$$

$$[Zn(OH)_4]^{2-} \longleftrightarrow ZnO_2^{2-} + 2H_2O \qquad (2.3)$$

$ZnO_2^{2-} + H_2O \longleftrightarrow ZnO + 2OH^-$ (2.4)

$ZnO + OH^- \longleftrightarrow ZnOOH^-$ (2.5)

The growth process could be described as follows (Kawska *et al.*, 2008). At the very beginning, the Zn^{2+} and OH^-ions coordinate with each other, and then they undergo dehydration by proton transfer, forming $Zn^{2+}\cdots O^{2-}\cdots Zn^{2+}$ bonds, and leading to an agglomerate of the form an hydroxyl complex of $[Zn_x(OH)_y]^{(2x-y)+}$,which has an octahedral geometry. The H_2O molecules formed by dehydration of Zn^{2+} and OH^-ions migrate into the solution. These aggregates usually contain fewer than 50 ions, and the formation of O^{2-} ions implies dramatic changes within the aggregate. After the aggregates reach around 150ions, wurtzite type (tetrahedral coordination) ZnO domains are then nucleated in the central region of the aggregates. The core comprisesZn^{2+} and O^{2-} ions only, while the aggregate surfaces till mainly consists of $Zn^{2+}$and OH- ions. Aggregates of over 200 ions exhibit a nanometer-sized core of the wurtzite structured ZnO which grows as a result of further association of Zn^{2+} and O^{2-} ions, and dehydration of $Zn^{2+}$and OH^-ions (Kawska *et al.*, 2008).In the above equations, the O^{2-} in ZnO comes from the base, not from the solvent H_2O. Therefore growth of ZnO does not necessarily require the solvent to beH_2O (Zhang *et al.*, 2002). It could be organic solvents, such as methanol (Cheng and Samulski 2004), ethanol (Liu *et al.*, 2003), and butanol (Cao *et al.*, 2006), and even ionic liquids (Alammar and Mudring, 2009). Under alkali conditions, the reactions could take place at room temperature by adjusting the ratio of Zn^{2+} and OH^-, giving rise to ZnO nanowires with diameter even below 10 nm. ZnO nanowires with various aspect ratios can be prepared by simply adjusting OH^-concentration and reaction time (Cao *et al.*, 2006).

2.7 Fabrication of ZnO/CNTs Nanocomposite

Recently, the studies of CNTs composited with other materials have been widely conducted and studied due to their remarkable properties and versatile applications.

Numerous synthetic methodologies for decorating ZnO with CNTs have been developed to bring about excellently enhanced electrical, optical and chemical properties (Rika *et al.*, 2015). Commonly, the methods of fabricating ZnO/CNTs nanocomposite are classified into:

i. single step (direct mixing) method
ii. multiple steps (sequence process) method.

Direct mixing of ZnO and CNTs nanomaterials to fabricate ZnO/CNTs nanocomposite is mostly done with the help of certain dispersant and polymer.

The direct mixing can be done by the use of a binder. Although this method is simple, however, the step of removing the binder at the end of synthesis process can lead to an ineffective process for the production of ZnO/CNTs nanocomposite and consequently, the desired morphologies of the nanocomposite may not easily be controlled (Du *et al.*, 2008).

The procedure of direct mixing followed by centrifugation with the assistance of different solvents such as diethyleneglycol, ammonia and de-ionized water were done by many researchers (Sui *et al.*, 2013).

The multiple steps are methods of fabricating ZnO/CNTs nanocomposite in multiple processes. Examples of this method include screen printing-pyrolysis, screen printing-CVD and sputter coating-CVD (Zhang *et al.*, 2009), and CVD- sputter coating (Wang and Chua 2012). Many multiple steps processes have been done to fabricate ZnO/CNTs nanomaterials as demonstrated in the following reports (Rika *et al.*, 2015).

Wang *et al*. (2008) reported the preparation of CNT/ZnO composites. Firstly, the CNTs (commercial CNTs) were treated with nitric acid (80%) at 80 ^oC for 4 h and washed with deionized water several times. $ZnCl_2$ (99%) was dissolved in deionized water, and $NH_3{\cdot}H_2O$ solution was slowly added under continuous stirring just when the white precipitate disappeared to form $Zn(NH_3)_4^{2+}$. Subsequently, the CNTs were added into the solution for 30 min. The mass ratio of $ZnCl_2$ and CNTs was 1:2. The products were separated from the solution using centrifuge, and dried at 70 ^oC in vacuum and the resulting products were calcined at 300 ^oC for 4 h at an atmosphere of nitrogen. SEM images revealed a flower-like ZnO structure with a central petal and six radial petals growing from the center and attaches on the tip of the CNT to form a CNT/flower-like ZnO heterojunction. Most of the flower-like ZnO structures are uniform with diameters from 600 nm to 1 mm and the surface of the flower is microscopically rough, but this rough surface consists of elongated particles rather than quasi-spherical ones.

Min *et al*. (2011) reported the fabrication of ZnO/CNTs nanocomposite using screen printing method. CNTs were mixed with ZnO in the presence of carboxymethylen cellulose (CMC). ZnO paste was initially prepared by mixing the ZnO powder with CMC, and CNTs were added in the paste and stirred to produce uniform ZnO/CNTs paste. The prepared paste was then printed on the substrates and annealed at 450˚C to enhance the crystallinity.

Compared to the other methods, screen printing method was suggested as the simplest and inexpensive method. However, in term of designing the morphology of ZnO/CNTs nanostructures and controlling the uniform dispersion through this method remains a challenge (Rika *et al*., 2015).

Klanwan *et al*. (2009) has reported a single-step synthesis of CNTs/ZnO nanocomposite using chemical vapour deposition (CVD) method. Pure zinc powder (99%, Merck) and glycerol–ferrocene mixture (Sigma-Aldrich) were loaded into two ceramic boats placed at different locations. Temperature profile with a designated maximal temperature of 1100 °C was determined with regard to the boiling point of glycerol, ferrocene (<300 °C) and zinc powder (907 °C). The boat of glycerol–ferrocene mixture was placed at the position of 5 cm while the zinc containing boat was at the position of 15 cm from the edge of the furnace. The growth of ZnO nanoparticles took place after the formation of CNTs. The as-synthesized products were oxidized by immersing in a 3:1 mixture of concentrated H_2SO_4 and HNO_3 with 1-h refluxing, following by refluxing in a concentrated HCl solution for another 1 h. Finally, the acid treated products were further refluxed in concentrated ammonia for 2 h and rinsed with deionized water for removing all residual ions. Electron microscopic analysis revealed that the fabricated nanostructures consisted of CNTs with a diameter of 60–70 nm which were coated with ZnO nanoparticles with an average size of 20–30 nm. The coated layer on the surface of the CNTs consists of a large number of much smaller ZnO nanoparticles with good crystallinity.

Liu *et al*. (2006) reported the formation of aligned CNTs and ZnO heterojunction through CVD. The CVD growth of the CNT–ZnO heterojunction arrays was carried out on a zinc foil supported by a quartz glass plate in a tube furnace at 850 °C under a combined flow of Ar (300 standard cubic centimetre per minute (sccm)), H_2 (20 sccm), and C_2H_2(10 sccm) for 10 min with a portion of the carrier gas passing through a water bubbler. This was then followed by purging the reaction system with a flow of argon (Ar) through the water bubbler for 20 min. SEM image showed that the ZnO nanoparticles were attached on the tip of each nanotube array.

Dutta and Basak (2009) reported on the fabrication of CNTs/ZnO nanowires (NWs) composite structures by following two steps method. First the ZnO NWs arrays are deposited on a glass substrate, and uniform CNT suspension was made by dispersing 0.4 mg of CNT (with an external diameter 20–40 nm and length 10–30 mm) in 30 ml of 2-propanol with the help of sodium dodecyl benzene sulfonate (SDDBS) yielded a stable dark suspension after the sonication of the solution for 45 min. The solution was centrifuged at 8000 rpm for 15 min and the clear supernatant liquid containing unbound SDDBS was discarded. This process was repeated few times and the final centrifugate was again suspended in 2-propanol. Secondly, a drop cast method was employed to cast a film of the suspended CNTs solution on the ZnO NWs. The CNTs' network was formed by increasing the number (n) of coatings. The composite structure shows enhanced ultraviolet emission and faster ultraviolet photo response time constants for multiple CNTs coatings (n = 5 and 2) compared to the bare ZnO NWs. The enhanced emission and faster photo response are correlated with the CNTs mediated surface plasmon resonance effect and faster electron transfer between the ZnO and the CNTs, respectively.

Shu *et al*. (2010) reported a new type of cathode film made of dendritic carbon nanotubes embedded with Zinc oxide quantum dots. The cathode film with dendritic structure carbon nanotubes embedded with zinc oxide quantum dots was prepared on the silicon substrates. Firstly, 10 gram ball milling zinc oxide nanoparticles were dispersed into30 ml terpineol solution. Secondly, 4 gram ethyl cellulose was dispersed in the above solution assistant with the ultrasonic so as to form the composite paste. Finally, the composite paste was then heated at 200 ^{o}C. After that the zinc oxide nanoparticles film was printed on the substrate through screen-printing process. The film thickness was about 10 microns. The film was sintered in the furnace at 560 ^{o}C to be growth substrate. Dendritic structure carbon nanotubes were grown on the composite film substrate through high-temperature pyrolysis of iron phthalocyanine chemical vapour deposition process. At last a new black film, which is about 1.5×1.5 square centimetre, was grown on the top of the substrate surface as the cathode. The dendritic structure looks like many small branches protrude from the main branches in SEM and TEM images, and both the branch and the trunk are embedded with Zinc oxide quantum dots.

Guadalupe *et al*. (2018) have reported CNTs decoration with ZnO using multiple steps method. The synthesis of ZnO nanoparticles on carbon CNTs was carried out in two stages. In the first stage, 5 mg of carbon CNTs were dispersed in 10 ml of dimethylformamide (DMF) by ultrasonication for 60 min. Then, 50 mg of Zn(ac) (zinc acetate dihydrate) and 24 μl/mL of thiophene (TP, as a capping agent) were added to a mixture of CNTs -DMF. Next, the mixture was kept in a sonicator for 1 h. Equal amounts of CNT and ZnO were used but thiophene concentration was varied in 2.6, 5, 10, 20, 40 μl/ml. In the second stage, the growth of ZnO nanostructures on carbon MWNTs was conducted in an ETHOS EZ Microwave Digestion System. The ZnO-CNTs-TP growth solution was irradiated for 15 minutes, maintaining a constant temperature of 160°C and 1000 W. The ZnO-CNTs product was separated from the supernatant by centrifugation and dispersed in ethanol; the process was repeated several times to wash out product impurities of the reaction. The resultant CNTs/ZnO nanocomposites were characterised by scanning and high-resolution transmission electron microscopy. It revealed that a significant portion of the surface of CNTs is covered with ZnO nanoparticles, and such particles form highly porous spherical nodules of 50-150 nm in diameter, sizes that are in values one order of magnitude larger than similar ZnO nanonodules. Hence, in the self-assembled nanocomposite the ZnO exhibits a large surface to volume ratio.

2.8 Principle of Characterization Techniques

2.8.1 Principle of scanning electron microscopy (SEM) technique

The Scanning Electron Microscope (SEM) is often the first analytical instrument used when a "quick look" at a material is required. In the SEM an electron beam is focused into a fine probe and subsequently raster scanned over a small rectangular area. As the beam interacts with the sample it creates various signals (secondary electrons, internal currents, photon emission, etc.), all of which can be appropriately detected. These signals are highly localized to the area directly under the beam. By using these signals to modulate the brightness of a cathode ray tube, which is raster scanned in synchronism with the electron beam, an image is formed on the screen. This image is highly magnified and usually has the “look "of a traditional microscopic image but with a much greater depth of field. With ancillary detectors, the instrument is capable of elemental analysis (Richard *et al*., 1992).

The SEM is closely related to the electron probe, is designed primarily for producing electron images. But can also be used for element mapping, and even point analysis, if an X-ray spectrometer is added. There is thus a considerable overlap in the functions of these instruments (Goldstein *et al.,* 2003).

2.8.2 Principle of energy dispersion spectroscopy (EDS) technique

The EDS makes use of the X-ray spectrum emitted by a solid sample bombarded with a focused beam of electrons to obtain a localized chemical analysis. All elements from atomic number 4 (Be) to 92 (U) can be detected in principle, though not all instruments are equipped for 'light' elements ($Z < 10$). Qualitative analysis involves the identification of the lines in the spectrum and is fairly straightforward owing to the simplicity of X-ray spectra. Quantitative analysis (determination of the concentrations of the elements present) entails measuring line intensities for each element in the sample and for the same elements in calibration Standards of known composition.

By scanning the beam in a television-like raster and displaying the intensity of a selected X-ray line, element distribution images or 'maps' can be produced. Also, images produced by electrons collected from the sample reveal surface topography or mean atomic number differences according to the mode selected (Subodh, 2006).

2.8.3 Principle of X-ray diffraction spectroscopy (XRD) technique

According to the Rutherford-Bohr model of the atom, electrons orbit around the positive nucleus. In the normal state the number of orbital electrons equals the number of protons in the nucleus (given by the atomic number, Z). Only certain orbital states with specific energies exist and these are defined by quantum numbers. With increasing Z, orbits are occupied on the basis of minimum energy, those nearest the nucleus, and therefore the most tightly bound, being filled first. Orbital energy is determined mainly by the principal quantum number (n). The shell closest to the nucleus ($n = 1$) is known as the K shell; the next is the L shell ($n = 2$), then the M shell ($n = 3$), etc. The L shell is split into three subshells designated L1, L2 and L3, which have different quantum configurations and slightly different energies (whereas the K shell is unitary). Similarly, the M shell has five subshells. This model of the inner structure of the atom is illustrated in Figure 2.5.

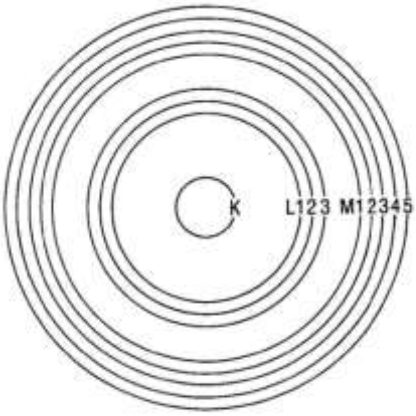

Figure 2.5: The model of the inner structure of the atom (Goldstein, 2003)

The populations of the inner shells are governed by the Pauli Exclusion Principle, which states that only one electron may possess a given set of quantum numbers. The maximum population of a shell is thus equal to the number of possible states possessing the relevant principal quantum number. In the case of the K shell this is 2, for the L shell 8, and for the M shell 18. Thus, for $Z \geq 2$ the K shell is full, and for $Z \geq 10$ the L shell is full. Electrons occupying outer orbits are usually not directly involved in the production of X ray spectra, which are therefore largely unaffected by chemical bonding etc.

2.8.4 UV-visible spectroscopy technique

UV-Visible Spectroscopy is a molecular spectroscopy that involves study of the interaction of Ultra violet (UV)-Visible radiation with molecules of a material. It measures the intensity of light passing through a sample (I) and compares it to the intensity of light before it passes through the sample (I_o). The ratio I/I_o is called the transmittance and is usually expressed as a percentage (%T). The absorbance, A, is based on the transmittance:

$$A = -\log\left(\%\mathrm{T}/_{100\%}\right) \tag{2.6}$$

When a beam of radiation strikes any object it can be absorbed, transmitted, scattered, reflected or it can excite fluorescence. These processes are illustrated in Figure 2.6. With scattering it can be considered that the radiation is first absorbed then almost instantaneously completely re-emitted uniformly in all directions, but otherwise unchanged. With fluorescence a photon is first absorbed and excites the molecule to a higher energy state, but the molecule then drops back to an intermediate energy level by re-emitting a photon. Since some of the energy of the incident photon is retained in the molecule (or is lost by a non-radiative process such as collision with another molecule) the emitted photon has less energy and hence a longer wavelength than the absorbed photon. Like scatter, fluorescent radiation is also emitted uniformly in all directions.

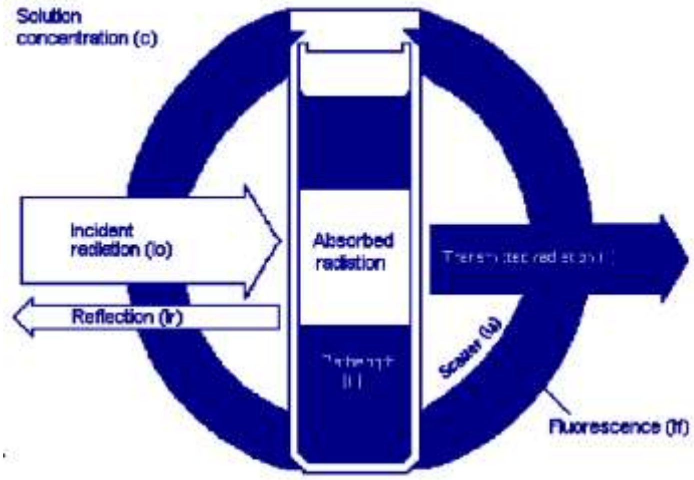

Figure 2.6: Principle of operation of UV-Visible Spectroscopy (Larry and Hanke, 2010).

The processes concerned in absorption spectrometry are absorption and transmission. Usually the conditions under which the sample is examined are chosen to keep reflection, scatter and fluorescence to a minimum. In the ultraviolet and visible regions of the electromagnetic spectrum, the bands observed are usually not specific enough to allow a positive identification of an unknown sample, although this data may be used to confirm its nature deduced from its infrared spectrum or by other techniques. Ultraviolet and visible spectrometry is almost entirely used for quantitative analysis; that is, the estimation of the amount of a compound known to be present in the sample. The sample is usually examined in solution (Larry and Hanke, 2010).

CHAPTER THREE

3.0 MATERIALS AND METHODS

3.1 Materials

The chemicals, apparatus and materials used for the synthesis of ZnO and fabrication of ZnO/CNT composites are presented in Table 3.1.

Table 3.1: Chemicals used for the synthesis of ZnO and fabrication of ZnO/CNT composites.

S/N	Name of chemical	Chemical compound	Brand	Purity (%)
1	Sodium hydroxide	NaOH	Aldrich	99.0
2	Zinc chloride	$ZnCl_2$	BDH	97.0
3	Ethanol	C_2H_5OH	JHD	99.5
4	Carbon nanotubes	CNT	Solaronix	-
5	Ruthenizer 535-bisTBA	N719		-
6	Acetone	C_3H_6O	MERCK	99.0
7	Hydrochloric acid	HCL	Aldrich	99.0
8	Deionized water	H_2O		

Table 3.2: The apparatus used for the synthesis of ZnO and fabrication of ZnO/CNT composites.

S/N	Name of apparatus	Source
1	Hydrothermal auctoclave	Instrumentation Lab. Niger Poly.
2	Homogenizer	Instrumentation Lab. Niger Poly.
3	Sonicator	Solid State Physics Lab. FUT Minna.
4	Magnetic stirrer	Instrumentation Lab. Niger Poly.
5	Hot air oven	Instrumentation Lab. Niger Poly.
6	Glass knife	Instrumentation Lab. Niger Poly.
7	pH meter	Instrumentation Lab. Niger Poly.
8	Weighing balance	Instrumentation Lab. Niger Poly.
9	Measuring cylinder	Instrumentation Lab. Niger Poly.
10	Stop clock	Instrumentation Lab. Niger Poly.
11	Beaker	Instrumentation Lab. Niger Poly.
12	Spatula	Instrumentation Lab. Niger Poly.
13	Funnel	Instrumentation Lab. Niger Poly.
14	Filter paper	Instrumentation Lab. Niger Poly.
15	Hand glove	Instrumentation Lab. Niger Poly.
16	Face mask	Instrumentation Lab. Niger Poly.
16	Sponge	Instrumentation Lab. Niger Poly.
17	Cotton wool	Instrumentation Lab. Niger Poly.
18	Clamp	Instrumentation Lab. Niger Poly.

3.2 Flow Chart of the Experimental Procedure of Hydrothermal Synthesis of as-synthesised ZnO and ZnO/CNT Composites.

3.2.1 Experimental Procedure

A flow chart of the procedures adopted in the experiment is given in Figure 3.1

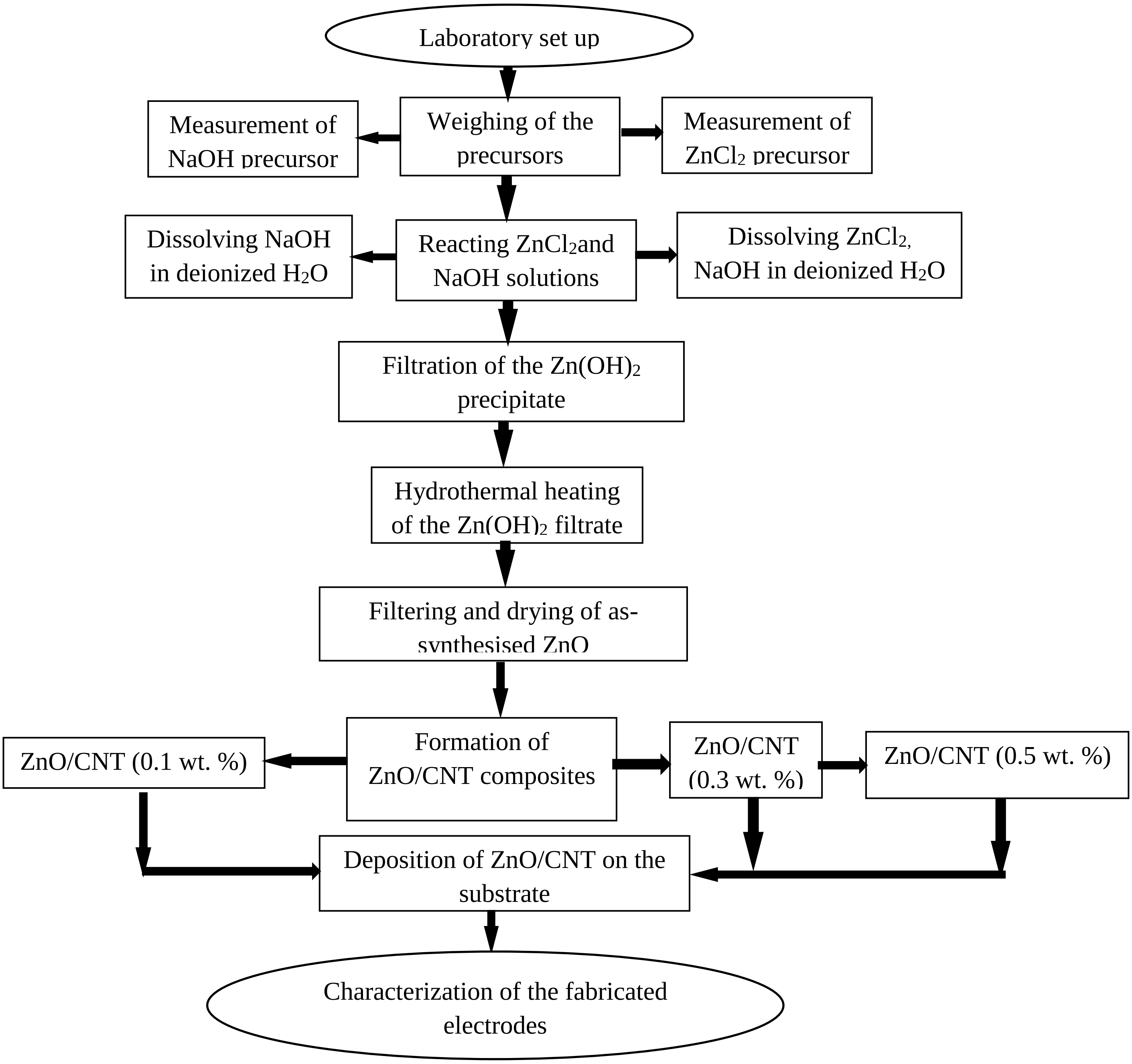

Figure 3.1: The experimental procedure in term of flow chart to depict the process of how hydrothermal synthesis of ZnO and fabrication of as-syntheised ZnO with CNT composites were achieved.

3.3 Methods

3.3.1 Synthesis of ZnO

In order to obtain accurate measurements of the precursors, equations (3.1) to (3.4) were employed to calculate the required mass of each precursor.

$$Molarity\ (M) = \frac{number\ of\ moles\ of\ solute\ (n)}{volume\ of\ solution\ (v)} = \frac{n}{v} \qquad (3.1)$$

but $$n = \frac{mass\ (m)}{molar\ mass\ (MM)} = \frac{m}{MM} \qquad (3.2)$$

substituting equation (3.2) into equation (3.1), we have

$$M = \frac{m}{MM} \times \frac{1}{v} \qquad (3.3)$$

So that when m in equation (3.3) is made subject of the formula, we have

$$m = M \times v \times MM \qquad (3.4)$$

where the unit of molarity (M) is (mol/ltr), mass (m) is (g), molar mass (MM) is (g/mol) and volume (v) is (ltr).

For $ZnCl_2$:

To prepare 1 M solution of $ZnCl_2$, 136.29 g of $ZnCl_2$ would be dissolved in 1 litre of solvent. Therefore, to prepare 0.5 M solution of $ZnCl_2$, **m** (g) of $ZnCl_2$ would be dissolved in 1 litre of solvent. If m_{ZnCl2} is the required mass of $ZnCl_2$ to get 0.5 M solution, we employ equation (3.5).

$$m_{ZnCl2} = M \times v \times MM \qquad (3.5)$$

where M = 0.5 mol/ltr, v = 1 ltr and MM = 136.29 g/mol. then

$$m_{ZnCl2} = 0.5 \times 1 \times 136.29$$

$$m_{ZnCl2} = 68.145\ g \qquad (3.6)$$

For NaOH:

To prepare 1 M solution of NaOH, 40 g of NaOH would be dissolved in 1 ltr of solvent. Therefore, to prepare 0.5 M solution of NaOH, **m** (g) of NaOH would be dissolved in 1 ltr of solvent. Ifm_{NaOH} is the required mass of NaOH, we employ equation (3.7).

$$m_{NaOH} = M \times v \times MM \tag{3.7}$$

where; M = 0.5 mol/ltr, v = 1 ltr and MM = 40 g/mol. then

$$m_{NaOH} = 0.5 \times 1 \times 40$$

$$m_{NaOH} = 20\,g \tag{3.8}$$

The mass ratio of $ZnCl_2$ to NaOH precursors was 1:4. This ratio emanates from the fact that higher concentration of alkaline compound (NaOH) than zinc salt compound ($ZnCl_2$) in the synthesis of ZnO, does not only promote but also aid complete formation of ZnO (Sheng and Zhong, 2014).

An electronic weighing balance (QY-G350900200D Scout Pro, USA) was used to measure $68.145\ g$ of $ZnCl_2$ and $80\ g$ of NaOH separately, as obtained in equations (3.6) and (3.8). They were then turned into a beaker containing less than 1litre of deionized water (which is the solvent) and later topped up to exactly 1 litre. The mixture was stirred continuously until the precursors were completely dissolved, forming a white precipitate of $Zn(OH)_2$. The white precipitate was filtered and washed using deionized water. The filtrate was then dispersed in deionized water and pH adjusted to between 11- 12 using hydrochloric acid (HCL) in drops. Having adjusted the pH, the mixture was stirred using a magnetic stirrer (Gallen Ramp, England) for 3 hrs and then turned into the Teflon-lining of a hydrothermal autoclave. The autoclave was coupled, and heated in a hot air oven (N53C, GenLab Widens, England) at 160 ^{o}C for 6 hrs. The oven was allowed to cool to room temperature and the autoclave brought out.

The heated mixture was filtered and washed using deionized water. The filtrate was then dried in a hot air oven at 60 ^{o}C for another 6 hrs.

3.3.2 Doping of ZnO with CNTs

0.1 wt% of CNT was added to a 50 ml beaker filled ethanol. The mixture of CNT-ethanol was subjected a dispersator (XHF-D High-speed Dispersator, China) for 30 minutes in order to avoid agglomeration of the nanotubes. The as-synthesised ZnO was added to the dispersed CNT and stirred at 80 ^{o}C using a magnetic stirrer until the ethanol was evaporated such that the mixture was a bit pasty. The prepared paste was ready for deposition onto the substrate. This process was repeated for 0.3 wt% and 0.5 wt% CNT concentrations.

3.3.3 Preparation of transparent conductive oxide (TCO) glass

The TCO glass is a glass plate coated on one side with a transparent conductive oxide (TCO) layer usually fluorine doped tin oxide (FTO). TCO glass plates are only conductive on one side. The conducting side was appropriately identified using a multimeter set by placing the mutimeter probes on the sides. The conductive side read a few ohms between 8-10 Ω when the probes are placed one milimeter apart in the middle of the FTO plane. Normally the conductive side is stronger and tougher than the non-conductive side of the glass. A line was inscribed on the TCO side of the glass at the desired position using a glass knife. After the cutting line is scribed, immediately, the glass was broken into two pieces by bending it outwardly from both sides of the line and hence the desired size acquired. A glass detergent was used to clean the delicate glass. After cleaning, the glass plates was rinsed thoroughly with deionized water and denatured alcohol to prevent traces of minerals. A hot-air blower was then used for faster drying.

3.3.4 The electrodes of ZnO and ZnO/CNT

The ZnO/CNTs electrode consists of a layer of ZnO/CNTs nanoparticles on a TCO glass substrate. Such a layer was obtained by the deposition of a paste containing a suspension of ZnO/CNTs particles. With the conductive side facing up, two parallel strips of tape were applied on the edges of the glass plate, covering about 5 to 7 mm of glass. The area of uncovered glass in the middle, is where the paste was deposited. The paste was deposited on the substrate using spin coating method.

The ZnO/CNTs electrode was completed by firing the deposited layer. This would leave the ZnO/CNTs nanoparticles sintered together. Sintering process ensures electrical contact between particles and good adhesion to the TCO glass substrate. Sintering can occur on a programmable hotplate. The adhesive tapes used for spin coating deposition were removed, and the freshly coated glass plate was placed on the hotplate at room temperature with its temperature set to 120 °C. After 1 hr, the baked ZnO/CNTs layer was looking whitish, indicating that the sintering process is over. The hot plate was allowed to cool before removing the fired electrode. A sudden change in temperature can cause the glass to break. The coated glass was also annealed at 350 ^{o}C for 30 minutes.

3.4 Characterisation Techniques

3.4.1 XRD

Structural analyses of the fabricated films of the as-prepared ZnO and ZnO/CNT films were performed using X-ray diffractometer (XRD, Rigaku D, Max 2500, Japan).

The X-ray diffractometer comprises of a monochromatic source of X-rays, sample holder, a diffractometer assembly, an X-ray detector and X-ray data analysis system.

The diffractometer assembly controls the alignment of the beam as well as the position and orientation of both the specimen and X-ray detector. The Rigaku D, Max 2500 diffractometer was used for the characterization of the prepared samples. Glass slide having a cavity of dimensions of 10x10x1mm^3 was used as a sample holder. Samples were fixed in this cavity with the help of a glass plate and then the sample holder was placed in the diffractometer for scanning. The diffracted rays make an angle of 2θ at the detector with respect to the incident beam direction. A scintillation counter was used as a detector and it was mounted on a diffractometer-goniometer stage. Power to the X-ray tube was switched on but voltage and current were increased slowly as were fixed at 30 kV and 15 mA, respectively. A shutter was also used with auto protection arrangement.

3.4.2 Optical ultraviolet-visible (UV-Vis) spectroscopy

Optical spectra were characterized using ultraviolet–visible light (UV–vis) spectrophotometer (Shimadzu UV-Visible Spectrophotometer, UV-1800 Series, Japan).

In its simplest form, the samples to be examined were placed between a light source and a photodetector, called cuvette, and the intensity of a beam of UV-visible light is measured before and after passing through the sample. The wavelength was varied between 200-900 nm at 0.5 nm intervals.

CHAPTER FOUR

4.0 RESULTS AND DISCUSSION

4.1 Synthesised ZnO

The synthesis of nanostructured ZnO using hydrothermal method was successful and was deposited on the FTO glass substrate to obtain the photoelectrodes of ZnO. The ZnO was later combined with CNTs at different percentage ratios of 0.1, 0.3 and 0.5 wt% to form nanocoposites of ZnO/CNT.

Table 4.1 summarizes the results of the calculated mass and volume of the chemicals used during the synthesis and fabrication of ZnO and ZnO/CNT nanocomposites.

Table 4.1: Summary of the calculations results used during synthesis and fabrication of the samples.

S/N	Precursor	Mass (g)	(wt%)	mL
1	$ZnCl_2$	68.145	-	-
2	NaOH	20	-	-
3	CNT first ratio	-	0.1	-
4	CNT second ratio	-	0.3	-
5	CNT third ratio	-	0.5	-
6	Deionized H_2O	-	-	1000
7	C_2H_5OH	-	-	20

4.2 Optical Measurement in the UV-Visible Region

4.2.1 Optical absorption spectrum

When a molecule absorbs energy, it excites an electron into a higher empty orbital hence ultraviolet and visible light can cause electronic transitions. Therefore, energy absorbance can be plotted versus the wavelength to obtain a UV-Visible spectrum. The UV-Visible spectrum shows the absorbance of a sample in the cuvette when scanned through various wavelengths in the UV-Visible region of electromagnetic spectrum. Both the shape of the peak(s) and the wavelength of the maximum absorbance (λ_{max}) give information about the structure of the sample. UV light has a wavelength which extends from 100~400 nm and visible light has wavelength range of 400~700 nm.

4.2.2 Transmittance (T) spectra

Figure 4.1 shows the optical transmission spectra of ZnO and ZnO/CNT composite thin films in the wavelength range from 200 to 900 nm. The spectra showed that the films were specular in the visible range of the electromagnetic spectrum. The film transmits from 237.65 nm to 290.82 nm then increased to 340.15 nm and broadens till 900 nm at 83 % transmittance value. This value proves that ZnO is a transparent conductive oxide material as it is a common saying amongst researchers (Akhavan *et al.*, 2011). Just as the as-synthesised ZnO film, other films also transmit from 237.65 nm. However, with the introduction of CNT, the transmission also increased from 237.65 nm to 324.83 nm, 326.21 and 340.15 nm and broadens till 900 nm for ZnO/CNT (0.1, 0.3 and 0.5 wt%) composite films at 79, 73 and 61 % respectively.

The optical transmittance spectra of the as-synthesised ZnO and ZnO/CNT films seem very similar and the transmittance in the UV region (310 - 380 nm) dropped slightly for all the films as this is the absorption region. In this region, the incoming photons have sufficient energy to excite electrons from the valence band to the conduction band and thus these photons are absorbed within the material to decrease the transmittance (Pradhan *et al.*, 2017). This region carries the information of the band gap of the material. In the visible region (380 -700 nm) and near infrared region (700 nm and above), the transmittance broadens and all the films showed transmittance from 83 % to 61 %. The variation of CNT content does not show significant change in transmittance in these regions. The slight decrease in transmittance with increasing CNT content might be due to the increment of scattering of photons by crystal defect (Hossain *et al*., 2018). These results imply that the optical transmittance can be enhanced by CNT incorporation in the ZnO thin film but incorporation of higher content may degrade the crystal quality which will eventually decrease the transmittance. This is similar to the works of (Pradhan *et al*., 2017; Xolani *et al*., 2017; Díaz-Corona *et al*., 2019; Aparimita *et al*., 2020).

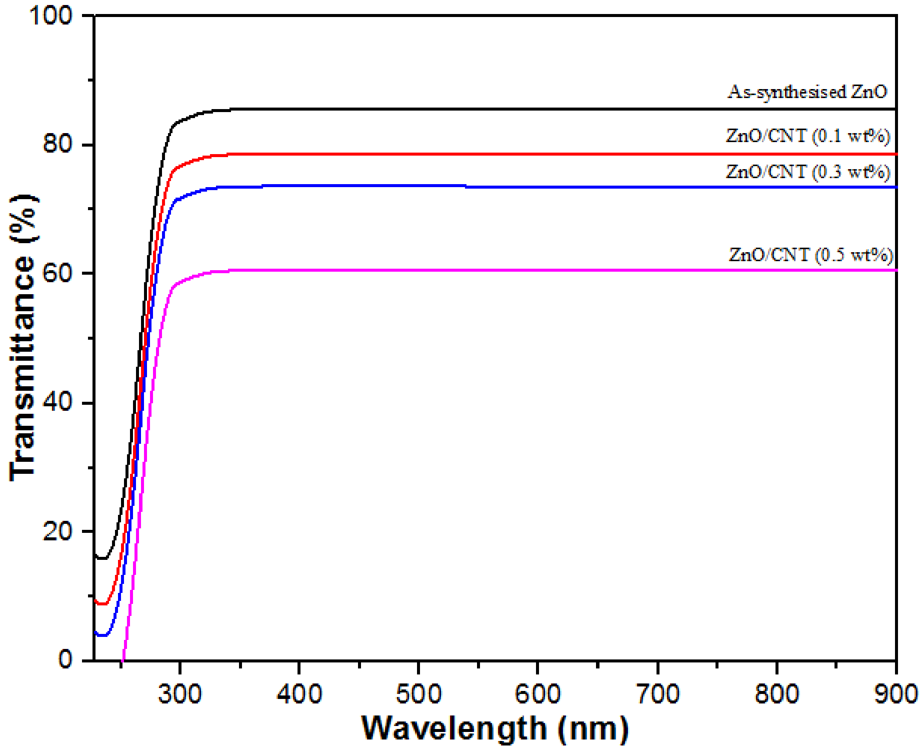

Figure 4.1: The transmittance spectra of the investigated ZnO and ZnO/CNT composites.

4.2.3 Reflectance (R)

The reflectance (R) spectra of ZnO and ZnO/CNT nanocomposite films are shown in Figure 4.2 (a-d). The as-synthesised ZnO film started reflecting light at 8.56 % and increased to 8.7 % at 274.27 nm before it later decreased to 8.43 % at 406.13 nm and again gradually increased till 8.44 % at 900 nm as shown in Figure 4.2 (a). When 0.1 wt% CNT was introduced into ZnO, the reflection of light was observed to start from 7.86 %, increased to 7.87 % at 274.27 nm just before it dropped 8.44 % at 406.13 nm and immediately, began rising till 7.74 % at 900 nm as seen in Figure 4.2 (b). This trend was replicated by ZnO/CNT (0.3 and 0.5

wt%) films. The reflection started at 7.36 % for ZnO/CNT (0.3 wt%) which decreased to 7.23 % at 402.71 nm just before it rises till 7.24 % at 900 nm as obvious in Figure 4.2 (c). In Figure 4.2 (d), 6.06 % of reflection value was observed at the beginning and dropped to 5.93 % at 376.10 which later begin rising again till 5.99 % at 900 nm. It is observed that in the UV region the reflectance increases smoothly for all the thin films and lies in the range of 8.56 % to 6.06 % just before it began to drop. The nature of increase gives an idea about the nature of the energy gap, which is ascertained further by the spectra of absorption coefficient. In the visible region, a gradual rise in the reflectance was observed for all the samples. The edge of these rises indicate the maximum reflectance value for the respective films. From both figures we see that, with the introduction of CNT content in the film, the reflectance of the film has a decreasing trend. It was gathered that the decreasing trend is due to local fluctuations of charged particles in the films. Reflectance decrease due to the interference between ZnO surface and the CNT which indicates the homogeneity and smoothness of the films (Shaaban *et al.*, 2013; Naik *et al.*, 2016). These results are strongly supported by the work (Wang *et al.*, 2017).

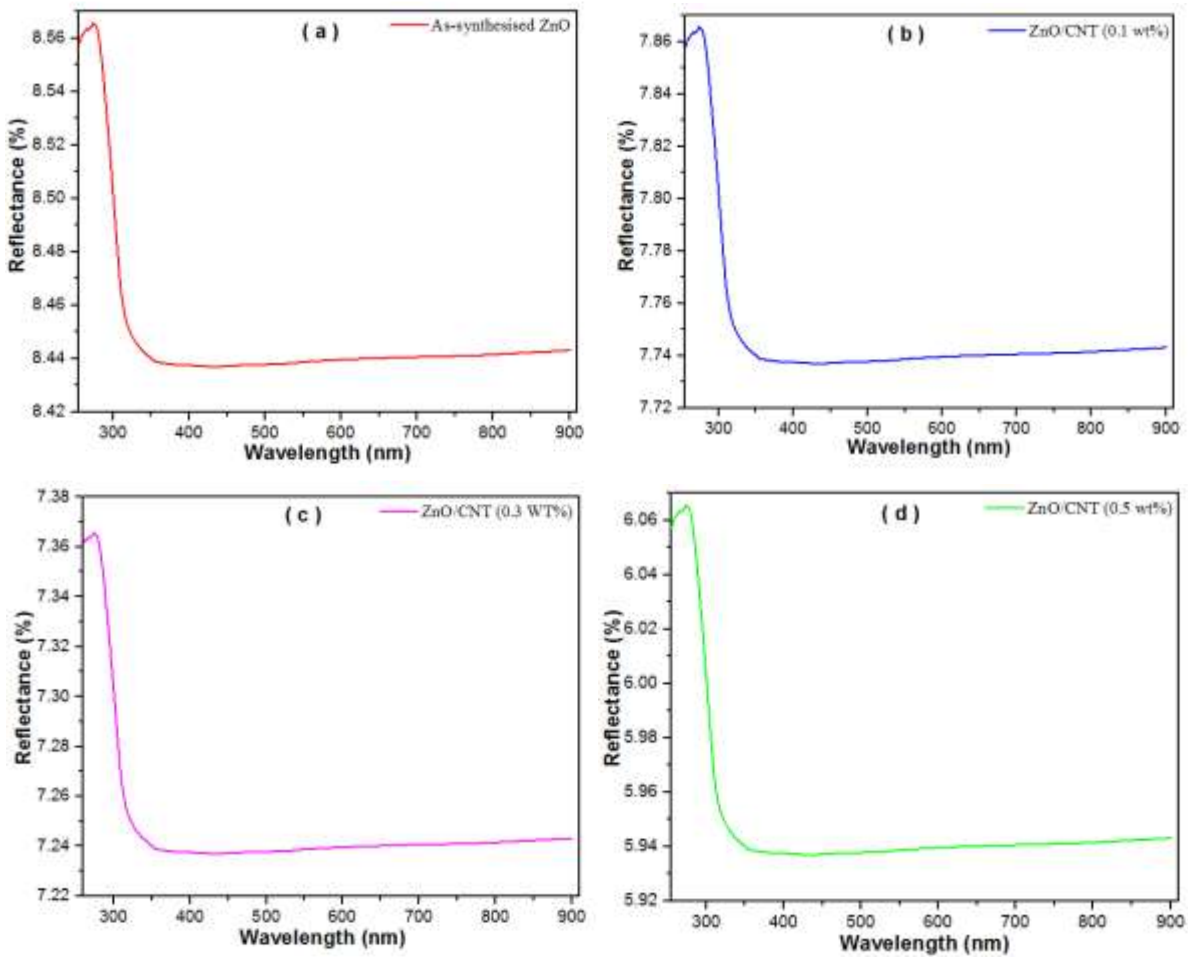

Figure 4.2: The variation of reflectance spectra as a function of wavelength for ZnO and ZnO/CNT films.

4.2.4 Absorption coefficient (α)

The optical absorption spectra data were used to evaluate the absorption coefficients, optical bandgap energies, band tail width and nature of transition involved in the films. The absorption coefficient characterizes how easily a material or medium can be penetrated by a beam of light (Hossain *et al.*, 2018). Absorption edge refers to the split-up energy between the lowest of the conduction band and the highest of the valance band that gives the optical band gap (Naik *et al*, 2016). The transmittance, reflectance and film thickness are related to the absorption coefficient by the relation given in Equation 4.1 (Ghanipour and Dorranian, 2013).

$$\alpha = \frac{1}{d} Ln\left[\frac{(1-R)^2}{2T} + \sqrt{\frac{(1-R)^2}{4T^2} + R^2}\right] \tag{4.1}$$

where:

α= the absorption coefficient

d= the film thickness

T= the transmittance

R= the reflectance

Figure 4.3 (a-d) shows the absorption coefficient (α) of the ZnO and ZnO thin films with different CNT concentrations. As seen in Figure 4.3 (a), the as-synthesised ZnO film started absorbing light at an absorption coefficient value of 1.0×10^5 cm^{-1} and gradually increased to 3.5×10^5 cm^{-1} where it linearly increased to 4.5×10^5 cm^{-1}. The ZnO/CNT films replicated a similar trend. ZnO/CNT (0.1 wt%) film started at 2.8×10^5 cm^{-1} absorption coefficient value and increased to 3.4×10^5 cm^{-1} before a linear increase to 5.1×10^5 cm^{-1} as shown in Figure 4.3 (b). Similarly, Zno/CNT 0.3 wt%) film had 0.4×10^5 cm^{-1} at the beginning and improved linearly to 4.9×10^6 cm^{-1} as seen in Figure 4.3 (c). It is also seen in Figure 4.3 (d) where the ZnO/CNT (0.5 wt%) had an absorption coefficient value of 0.68×10^6 cm^{-1} and improved gradually to 0.84×10^6 cm^{-1}. However, it dropped to 0.73×10^6 cm^{-1} and began icreasing linearly to an absorption edge of 2.1×10^6 cm^{-1}.

It is observed that the maximum absorption peak for ZnO film is 3.3 eV. Consequently, the introduction of CNT in to the ZnO film improved the absorption edge of the as-synthesised ZnO to 3.35 eV and 3.44 eV for 0.1 and 0.3 wt% CNT concentrations. However, the absorption edge of the film with 0.5 wt% CNT content was reduced to 3.32 eV. This indicates that after the absorption edge, the films become more transparent and the light wave can propagate faster and easier. These results are in agreement with the work (Díaz-Corona *et al.*, 2019).

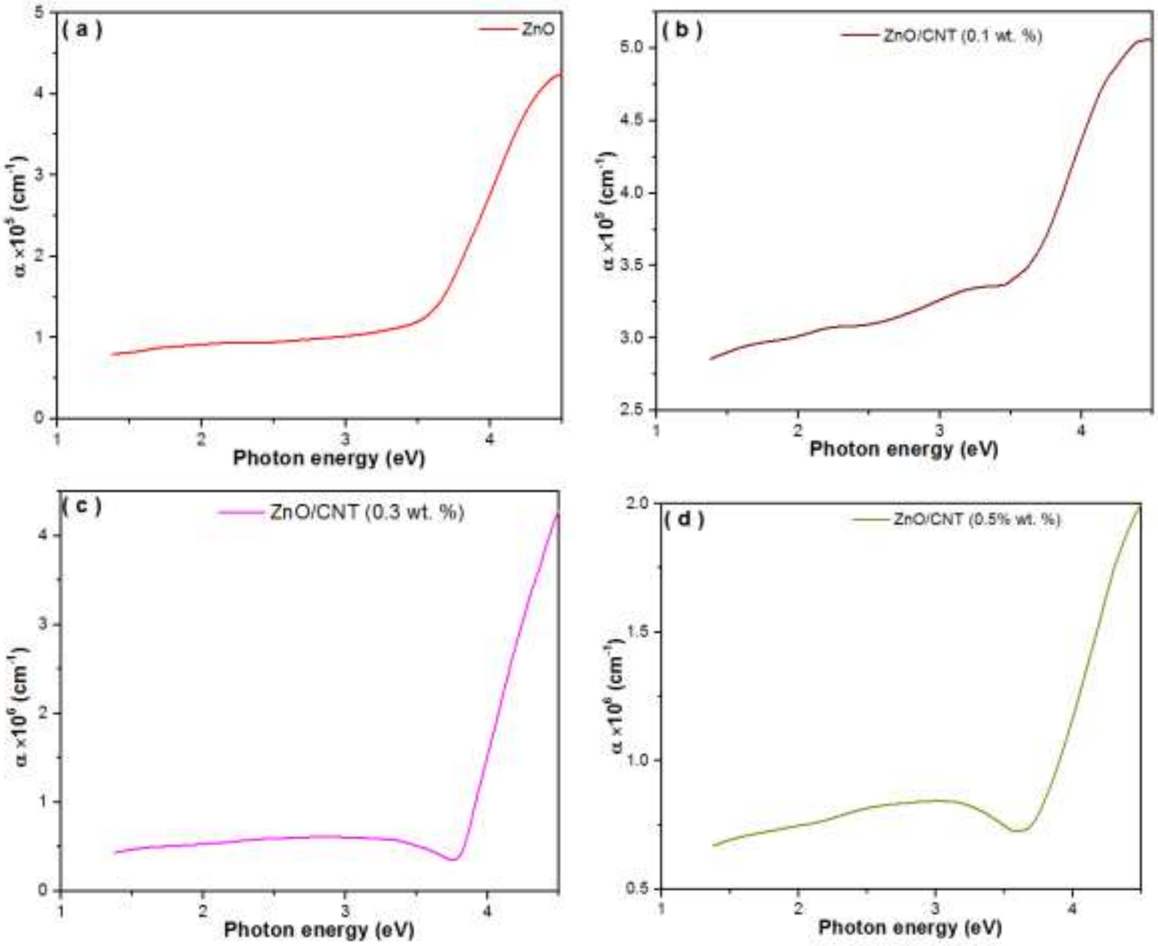

Figure 4.3: The optical absorption coefficients versus photon energies for (a) ZnO, (b) ZnO/CNT (0.1 wt. %), (c) ZnO/CNT (0.3 wt. %), and (d) ZnO/CNT (0.5 wt. %) films.

4.2.5 Extinction coefficient (k)

The extinction coefficient describes the properties of material with respect to light of a given wavelength and indicates the absorption changes when the electromagnetic wave propagates through the material (Ghanipour and Dorranian, 2013). The extinction coefficient (k) of the studied films was calculated by using the relation involving absorption coefficient and wavelength (Abdelraheem *et al*., 2020; Sahoo *et al*., 2020; Aparimita *et al*., 2020).

$$k = \frac{\alpha\lambda}{4\pi}$$

(4.2) where:

k= the material ability for polarization is shown in Figure 4.4.

α= the absorption coefficient

λ= the wavelength

Figure 4.4 shows the extinction coefficient plots against photon energy for the as-prepared ZnO and ZnO/CNT films. Figure 4.4(a) shows the maximum extinction coefficient of ZnO at 0.9. It was observed that the k value increased with photon energy as the concentration of CNT increased from 0.1, 0.3 to 0.5 wt. % as shown in Figures 4.4 (b), (c) and (d). The increase of k is due to the increase of charge carrier concentration as a result of surface absorption of CNT in the ZnO/CNT films. This is supported by the report of (Ghanipour and Dorranian, 2013; Naik *et al*., 2015; Sahoo *et al*., 2020).

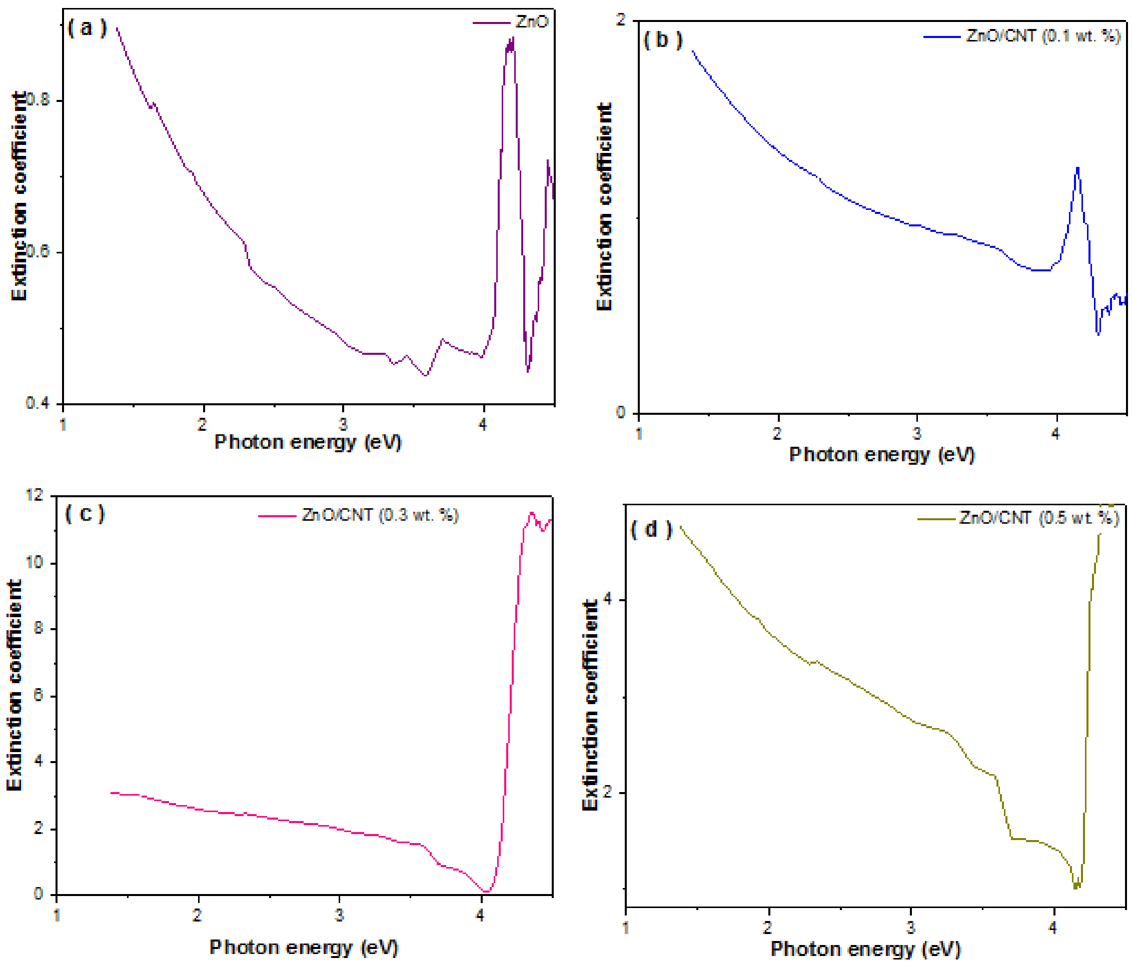

Figure 4.4: The extinction coefficient plots against photon energy for the ZnO and ZnO/CNT films.

4.2.6 Optical band gap (Eg) and tauc parameter

The optical band gap dependence of the absorption coefficient (α**)** is given by Equation 4.3 called Tauc and Davis-Mott relation. This relation is used to probe the optical band gap of nanoparticles from UV-Visible adsorption spectroscopy.

$$(\alpha hv)^2 = A\left(hv - E_g\right) \tag{4.3}$$

where:

α = is the absorption coefficient,

hv= is the incident photon energy,

n = is the nature of transition

A = is an energy independent constant (a parameter that depends on the transition probability also called Tauc parameter), and

E_g = is the optical band gap energy of nanomaterial.

The extrapolations of the linear part of the curve to the ‘’hv’’ axis can determine the E_g. The optical energy gap (E_g) and nature of band transition was obtained in the high absorption region by Tauc relation (Sahoo *et al.*, 2020).

The value of ‘n’ determines the mechanism of optical absorption whose value is $\frac{1}{2}$for direct allowed transition and 2 for indirect allowed transition (Behera and Naik, 2016; Hassanien and Sharma, 2019). The linear fitting of the data points of the linear portions by taking $n = \frac{1}{2}$ shows the direct allowed transition in the film. The plot of $(\alpha hv)^2$ versus (hv) gives a straight line and the intercept gives the optical band gap.

Table 4.2: Estimated values for bandgap (E_g) and Urbach energies (E_u) for the as-prepared ZnO and ZnO/CNT films.

S/N	Sample	E_g (eV)	E_u (meV)
1	ZnO	3.488	337
2	ZnO/CNT (0.1 wt. %)	3.257	367
3	ZnO/CNT (0.3 wt. %)	3.152	399
4	ZnO/CNT (0.5 wt. %)	3.013	446

Figure 4.5 shows the plot of $(\alpha hv)^{1/2}$ versus (hv) revealing how the values of E_g for the as-prepared ZnO and ZnO/CNT films were estimated. The estimated E_g values are presented in Table 4.2. The as-synthesised ZnO E_g was estimated to be 3.488 eV. This is very close to the conventional values of E_g 3.44 eV at low temperatures and 3.37 eV at room temperature for

ZnO (Janotti and Walle, 2011). Consequently, introduction of CNT in to the ZnO film varied the E_g values. The E_g values are 3.257, 3.152 and 3.03 eV for ZnO/CNT (0.1, 0.3 and 0.5 wt%) respectively. Incomplete healing during the annealing process is another possibility for the slight difference. This is in strong agreement with similar experimental results of 4.48 eV to 3.42 eV by (Lee *et al*., 2018).

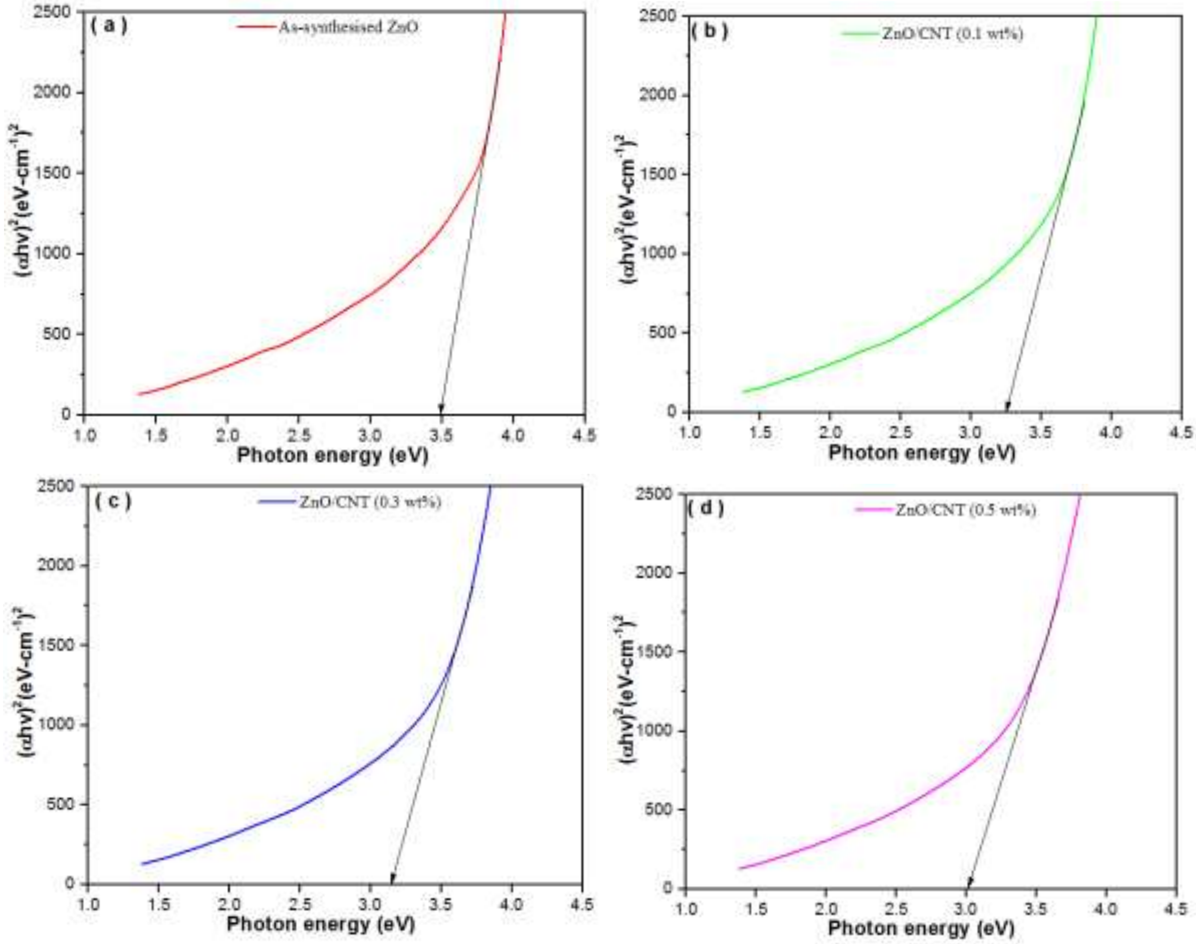

Figure 4.5: The plot of $(\alpha hv)^2$ versus (hv) for the as-prepared ZnO and ZnO/CNT films

As seen in Figure 4.5, it is observed that the *Eg* value of the ZnO/CNT film reduced with increasing concentration of CNT. This depicts that the electronic bands are expanded with the incorporation of CNT to ZnO (Guler *et al*., 2015). These results conform to the findings by others (Caglar and Yakuphanoglu, 2012; Serbetçi *et al*., 2012; Mansour and Yakuphanoglu, 2012).

4.2.7 Urbach energy

If an electron encounters a disordered state when in motion, the density of states of the electron decreases exponentially (decreases its tail) and enters the E_g from conduction band. The tail of the density of states that extends into the energy gap is called the Urbach tail, and the energy connected is described as Urbach energy (Boubaker, 2011; Chiodo *et al*., 2010). The absorption coefficient (α) in the lower absorption region depends exponentially on photon energy (hv) by Urbach relation.

$$\alpha(hv) = \alpha_0 \exp\left(\frac{hv}{E_U}\right) \tag{4.4}$$

where:

α_0= is a constant,

α = is the absorption coefficient,

h = is Planck's constant, and

E_U = is the Urbach energy.

By plotting a graph of $\ln\left(\frac{\alpha}{\alpha_0}\right)$ against (hv) and then the straight-line fitting to the curve gives the slope as $\left(\frac{1}{E_U}\right)$. The inverse of the slope gives the value of Urbach energy that represents the degree of disorder in amorphous materials.

Figure 4.6 shows the plot of ln(α) versus (hv) for the estimated E_u value for the as-prepared ZnO and ZnO/CNT films. The estimated E_u values are presented in Table 4.2. It is seen that the E_u varied slightly with increasing concentration of CNT from 337 meV for the as-synthesised ZnO to 367, 399 and 446 meV for 0.1, 0.3 and 0.5 wt% of CNT content respectively. This interprets to the increase in defect states in the localized region of the

ZnO/CNT films. The small value of Urbach energy translates to relatively low structural disorder which enhanced the crystalline quality of the films (Dibya and Mostako, 2020). The increase in E_u and decrease in Eg with increasing concentration of CNTs can be attributed to the slight increase of the degree of disorder that results in the increase of the band tailing, and consequently translates to the reduction of the band gap. This is similar to the work by (Pradhan*et al*., 2017; Atyia and Hegab 2016).

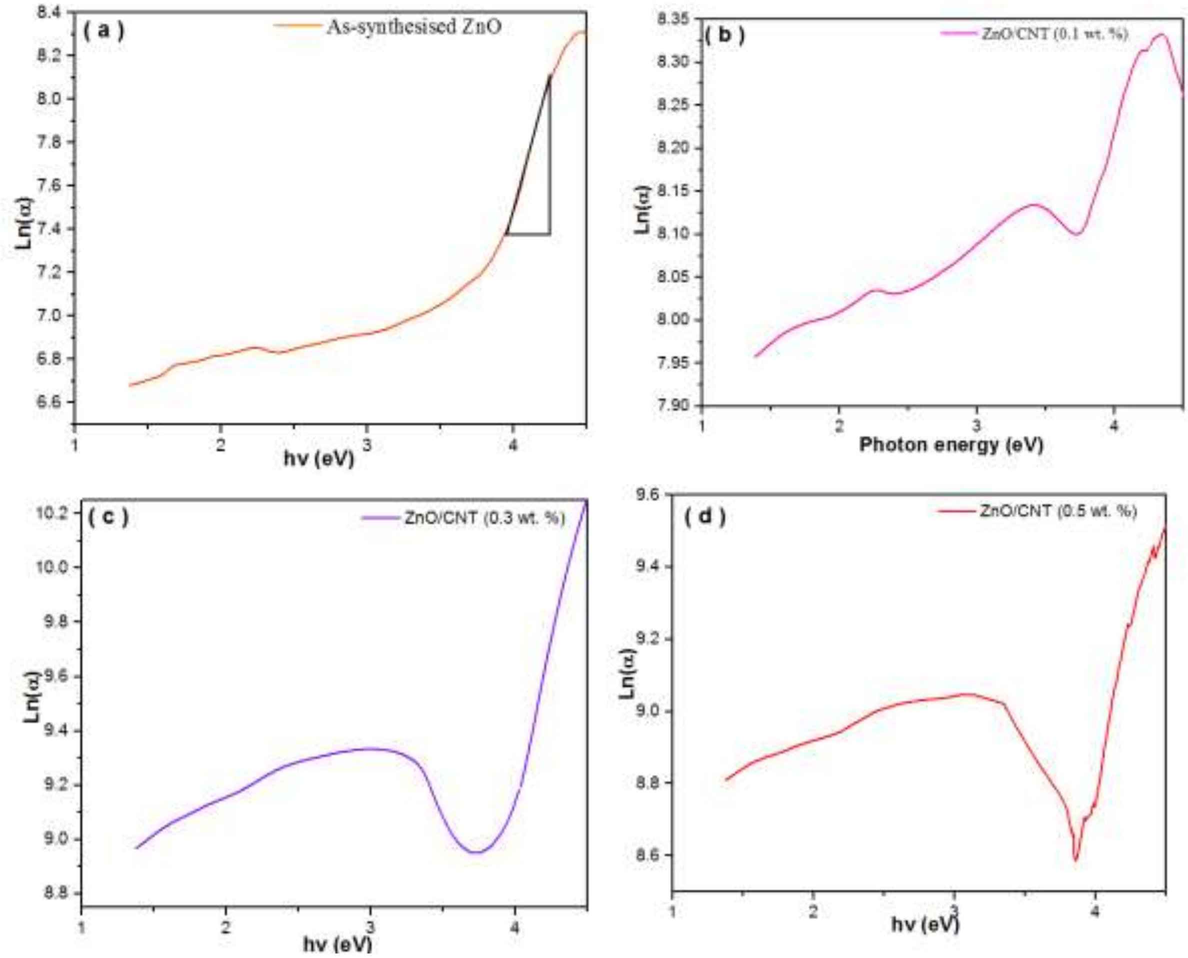

Figure 4.6: Plot of ln(α) versus (hv) for the estimation of E_u value for the as-prepared ZnO, ZnO/CNT (0.1, 0.3 and 0.5 wt. %) films.

4.2.8 Refractive index (n)

The refractive index (n) was calculated from the transmittance and reflectance spectra using Equation 4.4 (Kamble *et al*., 2011; Jena *et al*., 2013).

$$n = \left(\frac{1+R}{1-R}\right) + \sqrt{\frac{4R}{(1-R)^2} - k^2} \tag{4.5}$$

where n= is the refractive index, R= is the reflectance, and k= is the extinction coefficient.

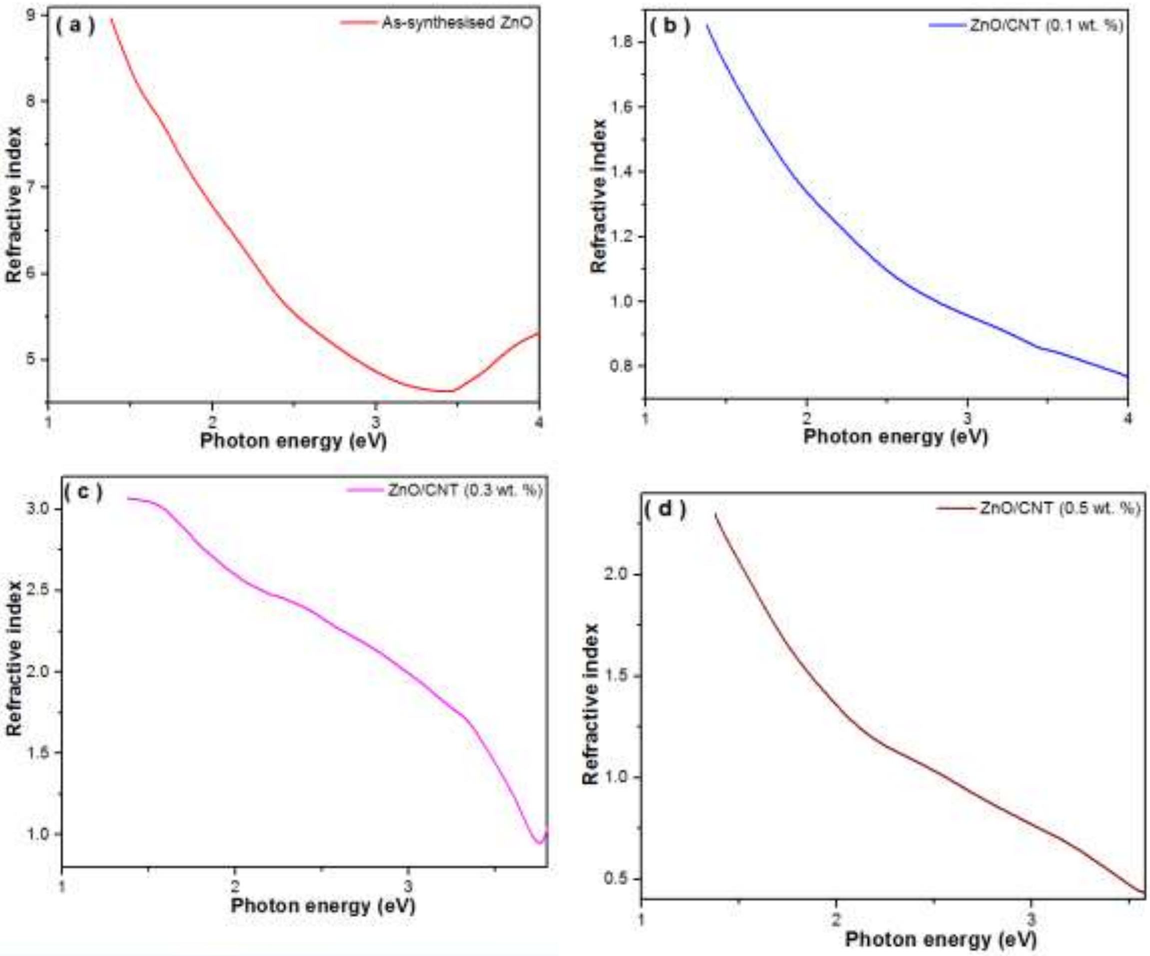

Figure 4.7: The plot of refractive index versus the photon energy for the as-prepared ZnO and ZnO/CNT films.

Figure 4.7 shows the plot of refractive index versus the photon energy for the as-prepared ZnO and ZnO/CNT films. It is seen that (n) varied with increasing photon energy for all the films. This is attributed to the decrease of absorption coefficient indicating the normal dispersion behaviour of the studied films. The as-synthesised ZnO film varied from 8.96 to 5.31. This trend is similar to the ones observed for 3.07-0.95 and 2.30-0.44 observed for ZnO/CNT (0.3 and 0.5 wt%) films respectively. However, the addition of 0.1 wt% CNT concentration to the as-synthesised ZnO, the refractive index was reduced from 1.86 to 0.77. In addition, the refractive index decreased with increasing concentration of CNT in to the ZnO film. However, in this study, oxygen was abundant due to the calcination process. Hence, the high refractive index of the as-synthesised ZnO film may be attributed to excess oxygen (Mohamed, 2012). The increase in Eg value is accompanied by the decrease of refractive index. This agrees with the work (Ezenwa, 2012; Mohamed, 2012; Attia *et al.*, 2013).

4.2.9 Optical conductivity (σ)

The optical conductivity is an important parameter to get knowledge about the electronic state in the material with the help of absorption coefficient and refractive index (El-Nahass *et al.*, 2015). The optical conductivity of a material is expressed as

$$\sigma = \frac{\alpha n c}{4\pi k} \tag{4.6}$$

where:

α= is the absorption coefficient,

σ= is the optical conductivity,

n= is the refractive index, and

k= is the extinction coefficient.

Figure 4.8 shows the variation of the optical conductivity versus wavelength for the as-prepared ZnO and ZnO/CNT films. It is observed that the optical conductivity for all the films decreased with increasing photon energy and increasing CNT concentration. The decrease in σ with increasing concentration of CNT may attribute to the decrease in absorption coefficient, localized states and defects by annealing of the films. This is similar to the work (Güler, 2016).

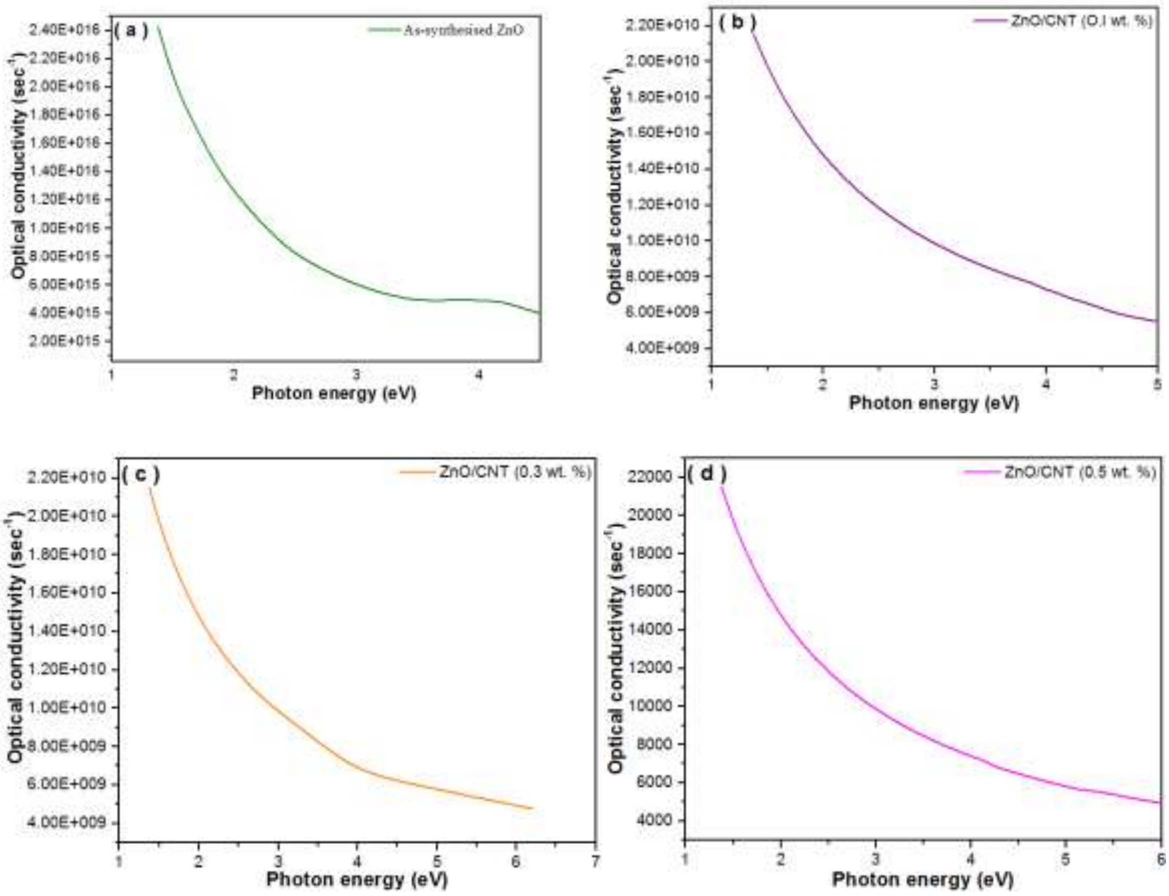

Figure 4.8: The variation of the optical conductivity versus wavelength for the as-prepared ZnO and ZnO/CNT films.

4.2.10 Dielectric constant (ε)

The complex dielectric constant $(\varepsilon = \varepsilon_1 - i\varepsilon_2)$ is considered as an intrinsic property of the material which is to be determined to improve the understanding of the optical properties. The real (ε_1) and imaginary (ε_2) part of the dielectric constant (ε) are related to the optical constants as:

$$\varepsilon_1 = n^2 - k^2 \tag{4.7}$$

$$\varepsilon_2 = 2nk \tag{4.8}$$

The real part represents the dispersion (how much the electromagnetic wave slows down) in the material whereas the imaginary part gives the dissipative rate of the wave (how a dielectric material absorbs energy from an electric field due to dipole motion).

The variations of the dielectric constant ε_1 versus photon energy (hv) is shown in Figures 4.9. As shown in Figure 4.9, the $\varepsilon_1$of all the films decreased with increasing energy while they increase with increasing concentration of CNT. The as-synthesised ZnO had a dielectric constant of 0.0018 and decreased with increasing photon energy. The ZnO/CNT (0.1, 0.3, 0.5 wt%) films had similar trend. The films with 0.1 and 0.5wt% of CNT concentration had dielectric constant of 1.55 and 1.3 respectively. However, when 0.3 wt% CNT was introduced, the film had a dielectric constant of 0.8 which is lower than that of 0.1 and 0.5 wt% CNT concentrations.

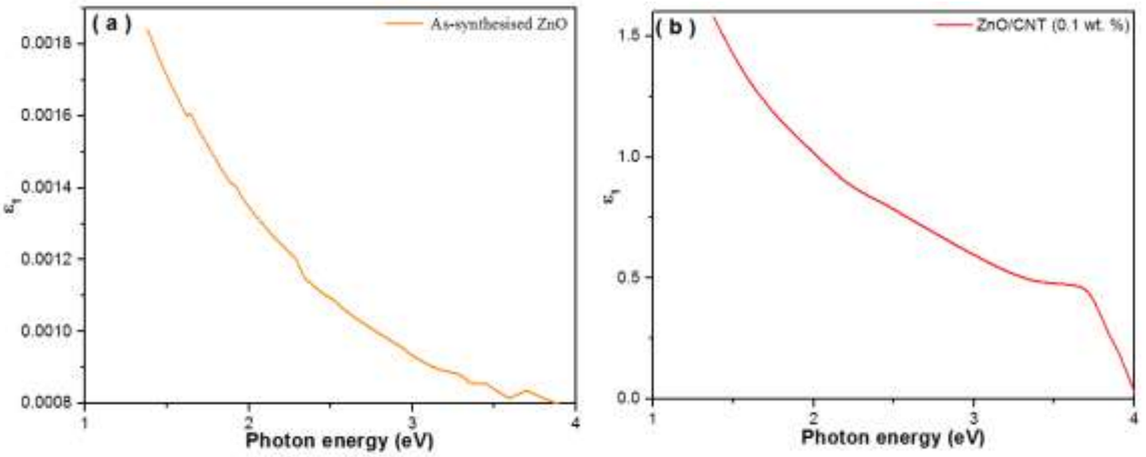

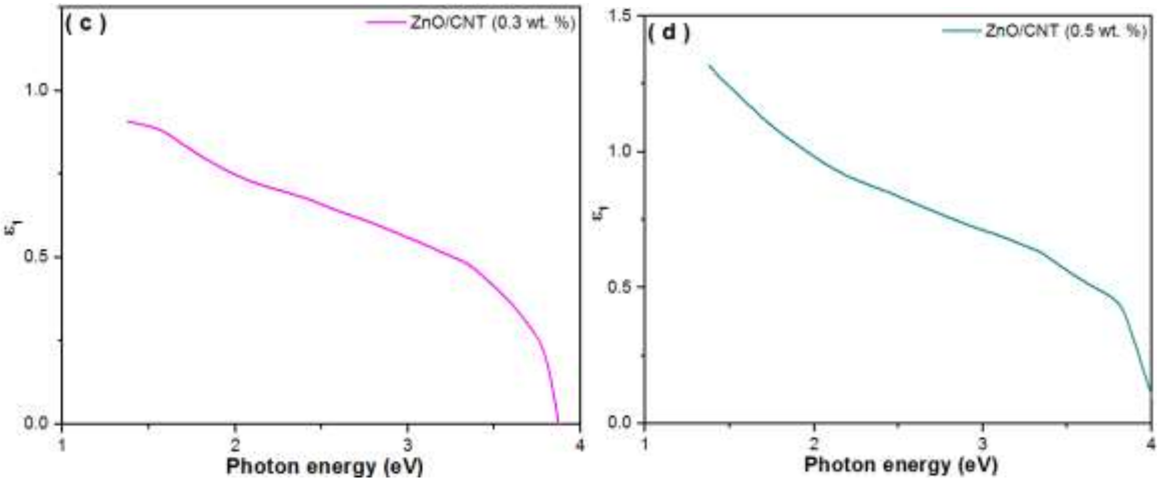

Figure 4.9: The dielectric constants ε_1 (real parts) versus photon energy (hv) for the as-prepared ZnO and ZnO/CNT films.

The variations of the dielectric constant ε_2 versus photon energy (hv) is shown in Figure 4.10. The dielectric constant (ε_2) of the as-synthesised ZnO decreased with increasing photon energy. A similar behaviour is exhibited by the ZnO/CNT (0.3 and 0.5 wt%) films. However, when 0.3 wt% CNT content was added, the film exhibited a behaviour such that the dielectric constant $\varepsilon_2$increased with increasing photon energy. These behaviours conform to the values of α and k for each film. These results are in accordance with the findings of (Wang *et al*., 2012).

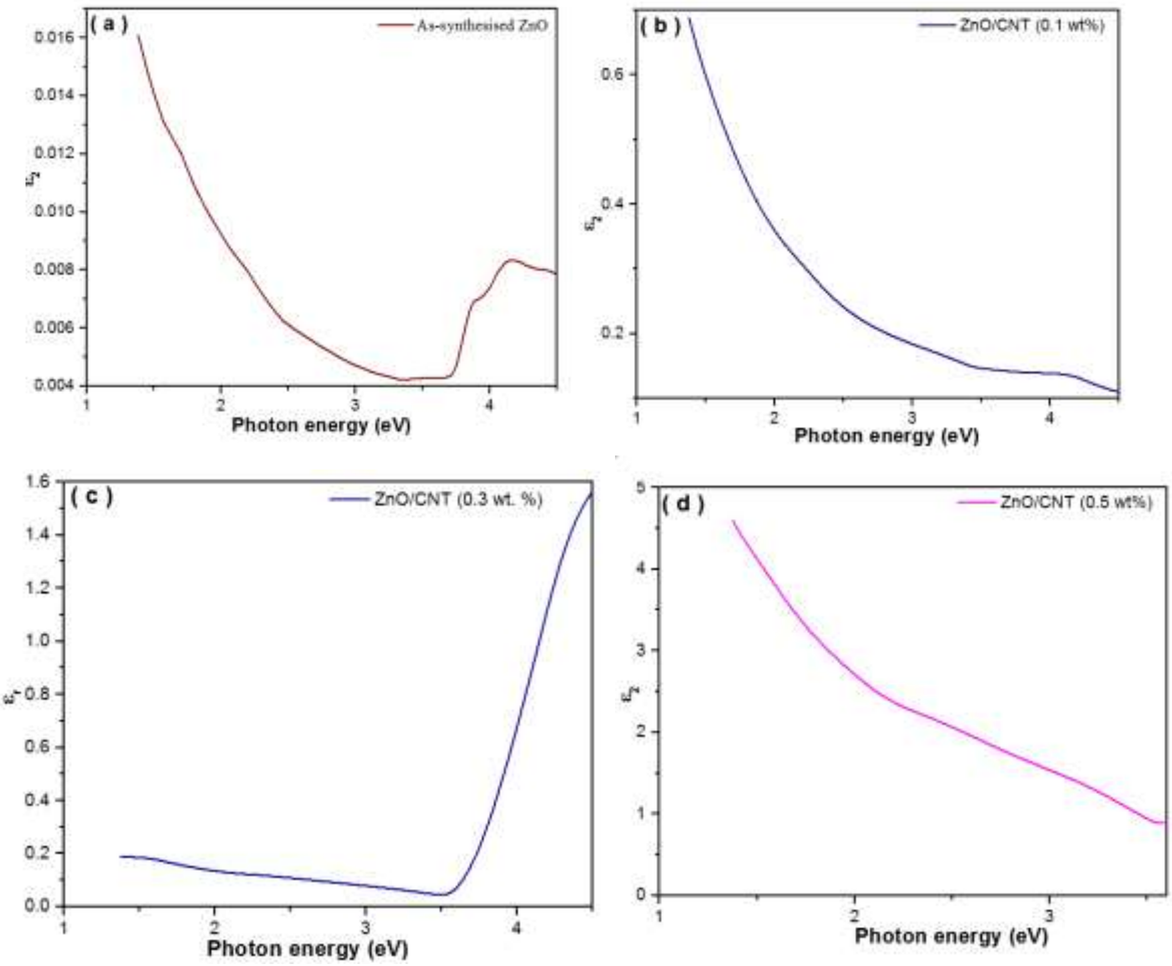

Figure 4.10: The dielectric constants $\boldsymbol{\varepsilon_2}$ (imaginary parts) versus photon energy (hv) for the as-prepared ZnO and ZnO/CNT films.

4.3 Dispersion Parameters

Investigation on the dispersion parameters and other optical constants of the as-synthesised ZnO and ZnO/CNT composite films was carried out.

The dispersion of the refractive index (n) is related to the incident photon energy (hv). The dispersion of (n) with (hv) below the optical absorption edge of the as-synthesised ZnO and ZnO/CNT films is given by Equations 4.9 and 4.10 as per Wemple-Di-Domenico (WDD) single effective oscillator model. The single-oscillatory model proposed by WDD describes the dielectric response for transitions below the inter-band absorption edge. Below the absorption edge, refractive index dispersion can be analysed by the single-oscillator model (Kasim, 2013 and Dibya and Mostako, 2020).

$$\left(n^2-1\right)=\frac{E_d E_o}{\left(E_0^2-(hv)^2\right)} \tag{4.9}$$

$$\left(n^2-1\right)^{-1}=-\frac{1}{\left(E_d E_o\right)}(hv)^2+\frac{E_o}{E_d} \tag{4.10}$$

Where E_o = is the single effective oscillator energy, which gives the quantitative information on the overall band structural of the material, and E_d = is the effective dispersion energy, which measures the average strength of inter-band optical transitions associated with the degree of structural order of the material.

Figure 4.11 shows plots of $\left(n^2-1\right)^{-1}$ versus $(hv)^2$ for the as-synthesised ZnO and ZnO/CNT composites films. The vital parameters that influence lattice absorption are single effective oscillator energy (E_o) and effective dispersion energy (E_d). The parameters 'E_o' and 'E_d' are estimated from the negative slope $\left(-\frac{1}{E_d E_o}\right)$ and y-axis intercept $\left(\frac{E_o}{E_d}\right)$ of the linear fit, and listed in Table 4.3 accordingly. The absence of any significant deviation from linearity in $\left(n^2-1\right)^{-1}$ versus $(hv)^2$ plot depicts there is no strong exciton peak below the inter-band edge (Dibya and Mostako, 2020).

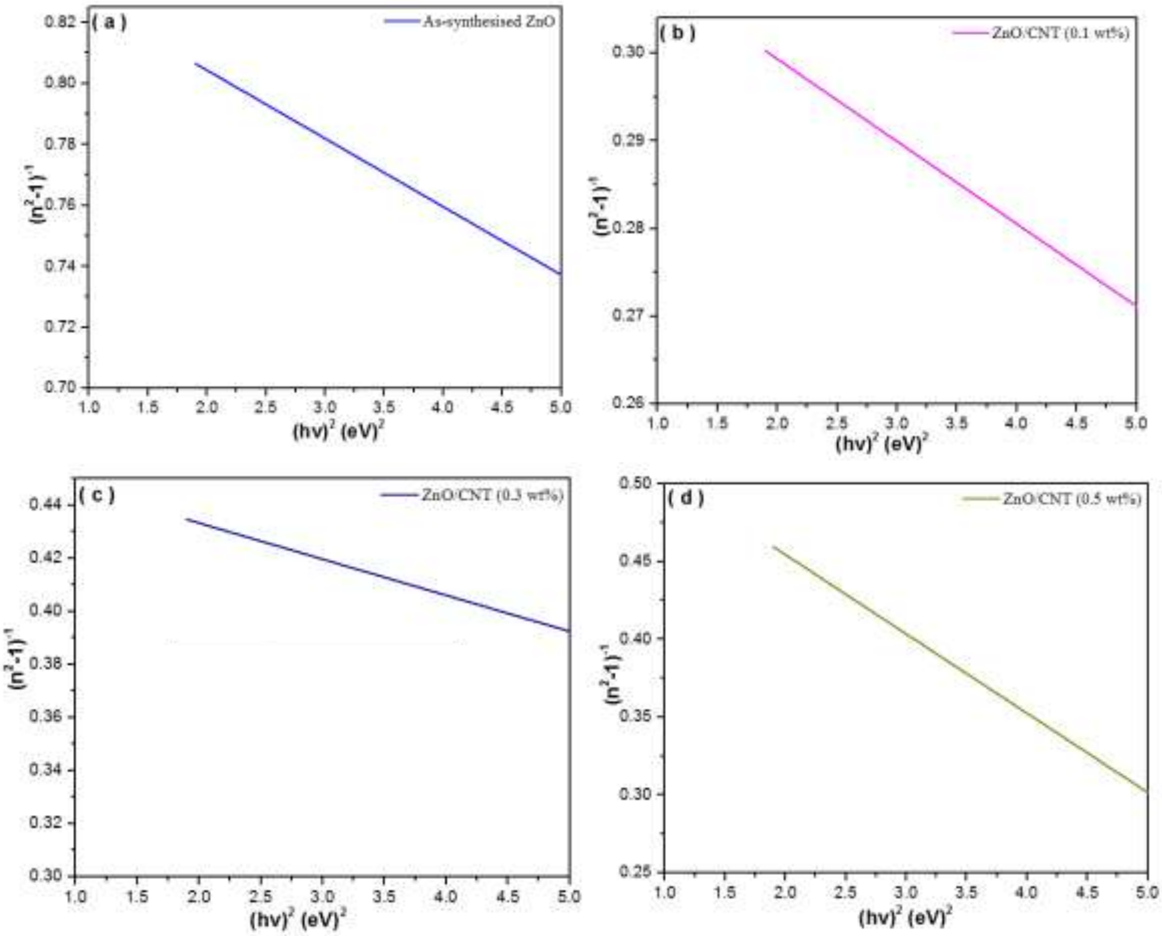

Figure 4.11: Plots showing the variation of $(n^2-1)^{-1}$ with $(hv)^2$ for the as-synthesised ZnO and ZnO/CNT films.

The values of E_o, E_d and E_o/E_g ratio are listed in Table 4.3. E_o value of 6.16 eV was obtained for the as-synthesised ZnO film. It is observed that the introduction of CNT content in concentration of 0.1, 0.3 and 0.5 wt% increased the E_o value of the as-synthesised ZnO to 12.64, 13.95 and 18.70 eV respectively.

E_d value of 7.25 eV was estimated for the as-synthesised ZnO film. However, the presence of 0.1, 0.3 and 0.5 wt% CNT content reduced the E_d value of the as-synthesised ZnO to 5.82, 4.24 and 1.05 eV respectively. The as-synthesised ZnO sample has the highest dispersion energy E_d of 7.25 eV, indicating it is of more ordered microstructure compared to other samples.

Since, the ratio of E_o/E_g signify the dopant driven defect that yield localized states around the energy band gaps and strongly influence the optical as well as structural properties of thin films. It is observed from Table 4.3 that 1.74 of E_o/E_g was obtained for the as-synthesised ZnO and increased to 3.63, 4.08 and 5.29 as 0.1, 0.3 and 0.5 wt% concentrations of CNT were added respectively. The deviation in the E_o/E_g values of the films varied with about ±1 eV. The increase of E_o/E_g with increasing CNT concentration indicates the improvement of the film quality, as confirmed by XRD analysis. Similar deviation in the values of E_o/E_g in a similar work in studying the optical properties of ZnO films had been reported (Dorgam *et al.*, 2016).

Based on the estimated values of 'E_o' and 'E_d', the static refractive index (n_0) of the as-synthesised ZnO and ZnO/CNT films is calculated by putting $(hv)^2 = 0$ in Equation 4.10 and it is reduced to Equation 4.11:

$$n_0 = \sqrt{1 + \frac{E_d}{E_o}} \tag{4.11}$$

The calculated values of "n_o" is also listed in Table 4.3. The n_0 calculated for the as-synthesised ZnO film was 1.47. It slightly dropped to 1.21, 1.14 and 1.03 when 0.1, 0.3 and 0.5 wt% CNT contents were introduced. It is observed that n_0 value decreased with increasing CNT concentration. This indicates improvement of crystalline microstructure which enhance the optical response of the material. Moreover, the values of static refractive indices estimated from WDD model are marginal to that obtained by (Durgam *et al.*, 2016).

Table 4.3: Estimated oscillator dispersion parameters of the as-synthesised ZnO and ZnO/CNT films.

Sample	**E_o (eV)**	**E_d (eV)**	**E_0/E_g**	**n_0**	**M_{-1}**	**M_{-3} ×10^{-3} (eV)$^{-2}$**
ZnO	6.16	7.25	1.74	1.47	1.177	42.97
ZnO/CNT (0.1 wt%)	12.64	5.82	3.63	1.21	0.460	0.609
ZnO/CNT (0.3 wt%)	13.95	4.24	4.08	1.14	0.304	0.144
ZnO/CNT (0.5 wt%)	18.70	1.05	5.29	1.03	0.056	0.016

Based on the single oscillator model, the single-oscillator parameters E_o and E_d are associated to the imaginary part ε_i of the complex dielectric constant and the M_{-1} and M_{-3} moments of the ε_i optical spectrum can be derived from the Equations 4.12 and 4.13 (Oriaku and Osuwa, 2009; Kasim, 2013):

$$E_o^2 = \frac{M_{-1}}{M_{-3}} \tag{4.12}$$

and

$$E_d^2 = \frac{M_{-1}^3}{M_{-3}} \tag{4.13}$$

The M_{-1} and M_{-3} moments were calculated using Equation 4.12 and 4.13, and the values obtained are given in Table 4.3. M_{-1}=0.177 was obtained for the as-synthesised ZnO film. The introduction of CNT content 0.1, 0.3 and 0.5 wt% increased it to M_{-1}=0.460, 0.304 and 0.056 respectively. The value increased with increasing concentration of CNT. However, a similar work where Co was doped with ZnO, had been reported (Petkova *et al.*, 2017).

M_{-3} moment for the as-synthesised ZnO was 42.92×10^{-3} (eV)$^{-2}$ and was reduced to 0.609×10^{-3} (eV)$^{-2}$, 0.144×10^{-3} (eV)$^{-2}$ and 0.016×10^{-3} (eV)$^{-2}$ when 0.1, 0.3 and 0.5 wt% CNT concentrations were introduced respectively. The M_{-3} moment decreased with increasing CNT concentration. This is in conformity with the work (Petkova *et al.*, 2017).

4.3.1 Linear dependence of n^2 on λ^2

In the absorption region, the square of refractive index (n^2) is related to the square of the wavelength (λ^2) by Equation 4.14 (Kasim, 2013):

$$\varepsilon_r = n^2 = \varepsilon_\infty - \left(\frac{e^2}{\pi c^2}\right)\left(\frac{N_c}{m^*}\right)\lambda^2 \tag{4.14}$$

where:

ε_r = the real part of the dielectric constant,

n^2 = the refractive index,

ε_∞ = the high frequency dielectric constant (or lattice dielectric constant),

e^2 = the electron charge,

c^2 = the velocity of light, and

$\left({N_c}/{m^*}\right)$ = ratio of free carrier concentration to free carrier effective mass.

The plot of n^2 against λ^2 is shown in Figure 4.12. It shows a linear dependence of n^2 on λ^2 in the transparent long wavelength region.

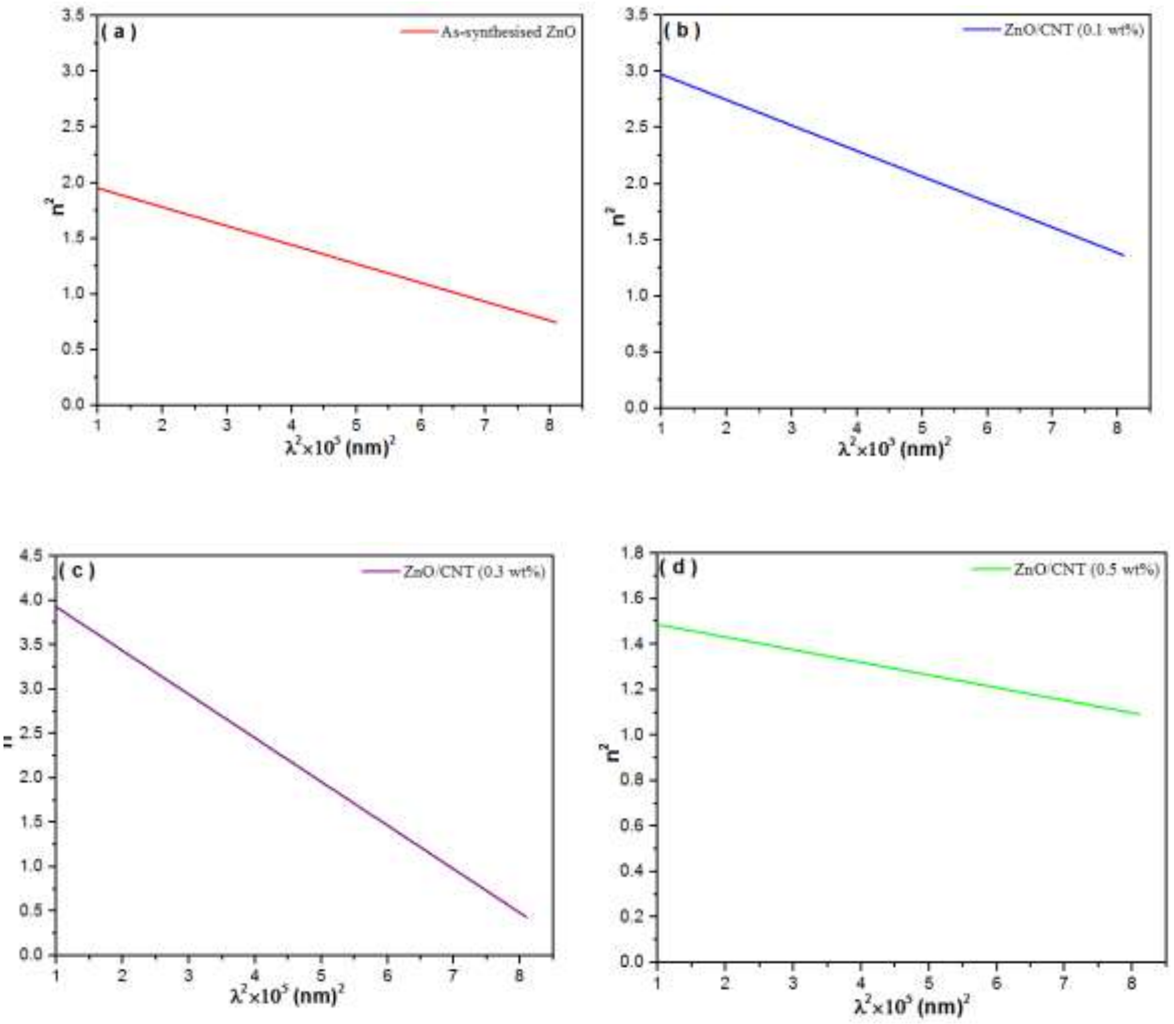

Figure 4.12: Plot of n^2 against λ^2 showing their linear dependence

Extrapolating the linear part of the plot to zero wavelength (that is, the intercept of the curve with n^2 axis at zero) gives the value of ε_∞ and N/m^* is determined from the slope. The values obtained are given in Table 4.4.

Table 4.4: Values calculated for ε_∞ and $N/m^*$of the as-synthesised ZnO and ZnO/CNT films.

Sample	ε_∞	**N_c/m^* ($\times 10^{49}$ $m^{-3}g^{-1}$)**
ZnO	2.12	1.9
ZnO/CNT (0.1 wt%)	3.19	2.5
ZnO/CNT (0.3 wt%)	3.96	3.6

ZnO/CNT (0.5 wt%)	1.54	6.1

The ε_{∞} value the as-synthesised ZnO estimated to be 2.12. It increased to 3.19, 3.96 and 1.54 with increasing concentration of CNT. The carrier concentration also increased with increasing concentration of CNT.

4.4 Structural Investigation using X-Ray Diffraction (XRD) Analysis

The existence of ZnO is generally in cubic zinc-blende and hexagonal wurtzite structural forms, and the CNT is in hexagonal rings form.

Figure 4.11 shows a typical XRD pattern of the as-prepared products of ZnO and ZnO/CNT thin films. The as-prepared thin films show polycrystalline with hexagonal structure of ZnO (ZnO: JCPDS 04-013-6608) (Gadallah and El-Nahass 2013). However, the as-prepared ZnO thin film has the strongest reflection at (101) plane which is the most prominent plane of the sample. On the other hand, it was observed that the pattern of the ZnO/CNT (0.1, 0.3 and 0.5 wt. %) films also have their strongest reflection at (101), the most prominent plane of the films. Reflections for planes (100), (002), (102), (110), (103), (002), (112) and (201) were also observed for both samples. Consequently, the (002) plane at $2\theta = 29.22^{o}$ evidently explains the presence of CNT. This plane was observed at a very low intensity for ZnO/CNT (0.1 wt%) film and improved as the concentration of CNT increased to 0.3 wt% CNT content. It became obviously pronounce in the 0.5 wt% CNT films. These results are similar to the ones obtained by (Yipeng *et al.*, 2008; Gadallah, 2013).

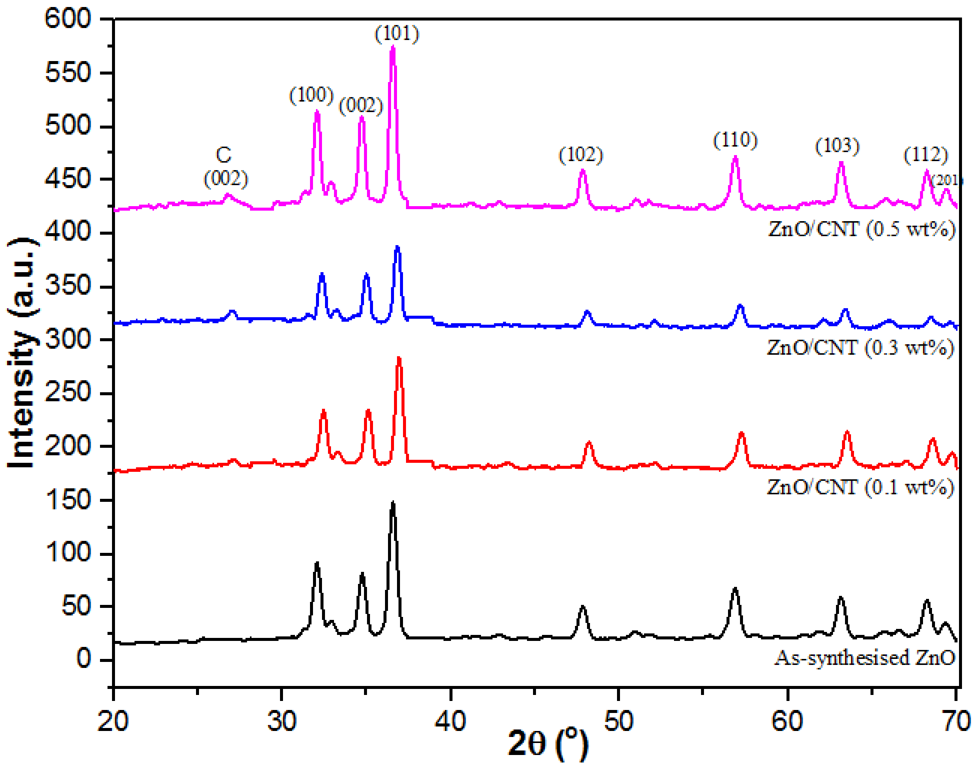

Figure 4.11: typical XRD patterns of the as-prepared products of ZnO and ZnO/CNT thin films.

Useful information that characterise the growth of ZnO and ZnO/CNT films were extracted from the XRD measurements. These include the crystallite size (D), defect density (δ), lattice strain (η), and stress (σ) of all the films.

4.4.1 Crystallite size (D)

The crystallite size (D) for each of the films have been calculated using Scherrer equation.

$$D = \frac{k\lambda}{\beta \cos\theta} \tag{4.9}$$

where:

D = crystallite size (nm),

κ = Scherrer constant (0.94),

λ= wavelength of the x-ray sources (1.5406 Å),

β = full width at half maximum (FWHM) of the diffraction peak (radians), and

θ = Bragg's diffraction angle or peak position (radians) (Gadallah and El-Nahass 2013).

Using Equation 4.8 and the data obtained from Figure 4.11, the crystallite sizes calculated for the as-synthesised ZnO and ZnO/CNT films are in Table 4.5.

4.4.2 Defect density (δ)

The defect density (δ), defined as the length of the dislocation line per unit volume, is given by

$$\delta = \frac{1}{D^2} \tag{4.10}$$

The calculated (δ) values for the as-prepared ZnO and ZnO/CNT films are shown in Table 4.5. The lower the dislocation density is, the better is the quality of the crystallized thin film.

4.4.3 Lattice strain (η)

The lattice strain (η) caused by mismatch between the glass substrate and the as-prepared ZnO and ZnO/CNT thin films is given by Equation 4.10.

$$\eta = \frac{\beta}{4\tan\theta} \tag{4.11}$$

The calculated (η) values for the as-prepared ZnO and ZnO/CNT thin films are shown in Tables 4.6, 4.7 and 4.8.

The lattice constants $a = b$ and c of the hexagonal structure are given by (Cullity and Rstock, 2001).

$$a = b = \frac{\lambda}{\sqrt{3} \times \sin\theta} \qquad (4.12)$$

$$c = \frac{\lambda}{\sin\theta} \qquad (4.13)$$

The calculated values of “*a”* and “*c”* for the as-prepared ZnO and ZnO/CNT films are shown in Table 4.5. The standard values of “*a”* and “*c”* for the hexagonal structure of ZnO are 3.253 and 5.215 Ǻ. Hence, these standard values are close to the values reported in here.

4.4.4 Residual stress (σ)

The residual stress (σ) in the as-prepared ZnO and ZnO/CNT thin films were determined by employing Equation 4.14.

$$\sigma = -233 \frac{c - c_0}{c_0} \text{ (GPa)} \qquad (4.14)$$

where:

c_0= 5.2066 Ǻ is the unstrained lattice constant for bulk ZnO (Bindu and Sabu 2014).

The obtained residual stress for the as-prepared ZnO/CNT and ZnO/CNT thin films are shown in Tables 4.6, 4.7 and 4.8. The minus sign indicates that the residual stress is compressive.

Table 4.5: The calculated values for average crystallite size (D) and defect density (δ) of the as-prepared ZnO and ZnO/CNT thin films.

Sample	D (nm)	δ ×10^{-4} (lines/nm^2)

ZnO	41.93	5.67
ZnO/CNT (0.1 wt%)	41.93	5.67
ZnO/CNT (0.3 wt%)	41.02	5.94
ZnO/CNT (0.5 wt%)	41.02	5.94

As seen in Table 4.5, the obtained average crystallite size for the as-synthesised ZnO film was 41.93 nm and remained unchanged when 0.1 wt% CNT content was added. However, the introduction of 0.3 and 0.5 wt% CNT content reduced the average crystallite size of the films to 41.02 nm.

As shown in Table 4.6, the 2θ values represent peaks where planes are reflected. It was observed that inter planar spacing value of the as-synthesised ZnO decreased with increasing 2θ. The full width at half maximum (FWHM) of the film reduced from 0.1968 rad. to 0.1574 rad. (which translates to sharpening of the peak at that position) and increased again to 0.2362 rad. (which means broadening of the peak at that position). An increase was also observed from 0.2362 rad. to 0.3149 rad. just before it reduced to 0.2362 rad. and again increased to 0.2755 rad. The broadening and sharpening of peaks as a result of fluctuations in the values of FWHM is a common observation amongst Tables 4.6 to 4.9. This behaviour is evidently obvious in Figure 4.11.

Table 4.6: Parametric values of FWHM (β), lattice strain (η), and residual stress (σ) for the as-prepared ZnO film

2θ (^{0})	**d-spacing (Å)**	**β (radian)**	**$\eta\times10^{-3}$**	**σ (GPa)**
32.081	2.72200	0.1968	2.987	-16.507
34.780	2.57945	0.1574	2.193	-2.326
36.547	2.36471	0.2362	1.821	-13.123
47.910	1.89877	0.2755	2.706	-63.197
56.814	1.62054	0.3149	2.54	-88.079
63.112	1.47313	0.3149	2.237	-101.261
68.200	1.37511	0.2362	1.522	-110.027
69.322	1.35557	0.2755	1.739	-111.774

Table 4.7: Parametric values of FWHM (β), lattice strain (η), and residual stress (σ) for the ZnO/CNT (0.1 wt%) film

2θ (^{0})	**d-spacing (Å)**	**β (radian)**	**$\eta\times10^{-3}$**	**σ (GPa)**
32.460	2.75830	0.1968	2.95	-2233.69
35.171	2.55172	0.1574	2.167	-2048.95
36.945	2.43315	0.3936	5.141	-1942.91
48.190	1.88838	0.3936	3.84	-1455.74
57.255	1.60909	0.3149	2.517	-1205.98
63.492	1.46522	0.3149	2.221	-1077.32
68.584	1.36834	0.3149	2.015	-990.676
69.726	1.27135	0.3014	1.888	-973.117

Table 4.8: Parametric values of FWHM (β), lattice strain (η), and residual stress (σ) for the ZnO/CNT (0.3 wt%) film

2θ (^{0})	**d-spacing (Å)**	**β (radian)**	**$\eta \times 10^{-3}$**	**σ (GPa)**
32.307	2.77108	0.2755	4.15	-2245.12
34.964	2.56633	0.1968	2.726	-2062.01
36.831	2.44040	0.1574	2.063	-1949.40
48.09	1.89210	0.3936	3.849	-1459.07
57.15	1.61180	0.2362	1.892	-1208.40
63.412	1.46689	0.3149	2.224	-1078.81
68.477	1.41817	0.4723	3.028	-992.36
69.549	1.39821	0.4723	2.968	-975.79

Table 4.9: Parametric values of FWHM (β), lattice strain (η), and residual stress (σ) for the ZnO/CNT (0.5 wt%) sample

2θ (^{0})	**d-spacing (Å)**	**β (radian)**	**$\eta \times 10^{-3}$**	**σ (GPa)**
32.0497	3.29079	0.43123	6.551	-16.74
34.6943	2.56633	0.42279	5.906	-1.77
36.5337	2.49912	0.44426	5.873	-13.04
47.8341	2.44040	0.54658	5.378	-62.94
56.8434	2.34813	0.68836	5.55	-88.15
63.1432	1.89210	0.77112	5.475	-101.32
68.2338	1.61180	0.65508	4.219	-110.08
69.3896	1.46689	0.77856	4.907	-111.88

The standard values of the lattice parameters a = b = 3.249 Ǻ and c = 5.205 Ǻ for bulk ZnO had been reported (Dorgam *et al.*, 2016). The values of lattice parameters a = b and c have been calculated for the prominent peaks for each of the samples using Equations 4.12 and 4.13, and are given in Tables 4.10, 4.11 and 4.12 respectively.

As shown in Table 4.10, 4.11, and 4.12 the inter planer spacing of the as-synthesised ZnO, for each peak, narrowed with the introduction of CNT. This means that the CNTs enter in to the lattice of ZnO, hence depicts improvement of crystallinity by reduction of structural disorder of the films with the increase in CNT concentration. This is similar to the work of (Dibya and Mostako, 2020).

The β values as given in Tables 4.10, 4.11 and 4.12, for the as-synthesised ZnO, shoot up with the presence of CNT. This means that the FWHM of the peaks broadened as the concentration of CNT increased. This behaviour was common for each of all the peaks.

Table 4.10: First prominent peak positions, β values and calculated lattice parameter (a=b and c) values of the as-synthesised ZnO and ZnO/CNT samples.

Sample	**Peak (^{0})**	**d-spacing (Å)**	**β (radian)**	**$\eta \times 10^{-3}$**	**a=b (Å)**	**c (Å)**	**D (nm)**
ZnO	36.547	2.4587	0.1378	1.821	3.0	5.0	55.6
ZnO/CNT (0.1 wt%)	36.945	2.4404	0.1574	5.141	3.0	5.0	44.0
ZnO/CNT (0.3 wt%)	36.831	2.4331	0.3936	2.063	3.0	5.0	55.6
ZnO/CNT (0.5 wt%)	36.534	2.3481	0.4442	5.873	3.0	5.0	19.6

Table 4.11: Second prominent peak positions, β values and calculated lattice parameter (a=b and c) of the as-synthesised ZnO and ZnO/CNT samples

Sample	**Peak (^{0})**	**d-spacing (Å)**	**β (radian)**	**$\eta \times 10^{-3}$**	**a=b (Å)**	**c (Å)**	**D (nm)**
ZnO	32.081	2.7900	0.1968	2.987	3.219	5.575	21.0
ZnO/CNT (0.1 wt%)	32.460	2.7710	0.1968	2.950	3.182	5.512	21.0
ZnO/CNT (0.3 wt%)	32.307	2.7583	0.2755	4.15	3.197	5.537	20.0
ZnO/CNT (0.5 wt%)	32.049	2.7110	0.43123	6.551	3.222	5.580	20.0

Table 4.12: Third prominent peak positions, β values and calculated lattice parameter (a = b and c) values of the as-synthesised ZnO and ZnO/CNT samples

Sample	**Peak (^{0})**	**d-spacing (Å)**	**β (radian)**	**$\eta \times 10^{-3}$**	**a=b (Å)**	**c (Å)**	**D (nm)**
ZnO	34.780	2.5794	0.1574	2.193	3.0	5.154	22.0
ZnO/CNT (0.1 wt%)	35.171	2.5663	0.1574	2.167	3.0	5.099	20.0
ZnO/CNT (0.3 wt%)	34.964	2.5517	0.1968	2.726	3.0	5.128	22.0
ZnO/CNT (0.5 wt%)	34.694	2.4404	0.42279	5.906	3.0	5.167	20.5

4.4.5 Unit cell volume (V)

Unit cell volume for hexagonal ZnO thin films has been calculated using (Gautam *et al.*, 2014):

$$v = \frac{\sqrt{3}}{2} a^2 c \tag{4.15}$$

where "a" and "c" are the lattice constants for ZnO nanocrystalline film. Table 5 lists the calculated values of unit cell volume for all the samples. It is apparent that that the Sample-3 has the smallest unit cell volume as compared to the standard. It is a consequence of higher stress in Sample-3 which resulted in reduction in unit cell volume.

4.4.6 Internal parameter (u')

The internal parameter u' is defined as the length of bond parallel to the c-axis (anion-cation bond length or the nearest neighbour distance) divided by the "c" lattice parameter and has been evaluated using Equation (4.16) (Gautam *et al.*, 2014) and the values are tabulated in Table 4.13.

$$u' = \left(\frac{1}{3}\right)\left(\frac{a^2}{c^2}\right) + \frac{1}{4} \tag{4.16}$$

4.4.7 Bond length

The bond length in c-direction has been calculated as U’c and the other three for the Wurtzite crystal structure (Gautam *et al*., 2014) by:

$$\left[\frac{a^2}{3}+\left(\frac{1}{2}-u'\right)^2 c^2\right]^{\frac{1}{2}} \tag{4.17}$$

The values are summarized in Table 4.13, where “a” and “c” are the lattice constants for ZnO nanocrystals.

Table 4.13: Calculated values of unit cell volume (v), internal parameter (u’), bond length in c-direction (U’c) and bond length in other three direction for all the films.

Sample	Peak	V (Å^3)	U’	U’c (Å)	U’ in other three direction (Å)	Density of film (g/cm^3)
ZnO	1st	50.0285	0.36112	2.01330	3.86535	5.403
	2nd	47.1792	0.36289	1.87071	3.57596	6.728
	3rd	48.9711	0.37000	1.85000	3.47527	6.936
ZnO/CNT (0.1 wt%)	1st	48.3444	0.36111	1.99046	3.82168	5.591
	2nd	48.2755	0.36111	1.84139	3.53546	7.063
	3rd	47.8386	0.36111	1.75582	3.37117	8.146
ZnO/CNT (0.3 wt%)	1st	49.0195	0.36111	1.99968	3.83938	5.514
	2nd	48.9368	0.36111	1.85193	3.55570	6.942
	3rd	47.4816	0.36111	1.76106	3.38122	8.074
ZnO/CNT (0.5 wt%)	1st	50.1758	0.36111	2.01528	3.86934	5.388
	2nd	49.8225	0.36111	1.86587	3.58246	6.788
	3rd	48.2769	0.36111	1.77489	3.40779	7.887

As shown in Table 4.13, the calculated unit cell volume, the bond length in c-direction and in other three direction for all the peaks decreased while the internal parameter and the film density increased with increasing 2θ position. This trend is common for all the films. However, the internal parameter remain unchanged for all the peaks of 0.1, 0.3 and 0.5 wt% CNT content films.

CHAPTER FIVE

5.0 CONCLUSION AND RECOMMENDATIONS

5.1 Conclusion

Nanostructured ZnO was synthesised using hydrothermal method and ZnO/CNT composites were fabricated. The effect of CNTs on the structural, morphological and optical properties was systematically studied. Structural and morphological analyses were carried out using XRD while optical properties were explored using UV-Visible Spectroscopy.

The as-synthesised ZnO was polycrystalline as evidently shown by the XRD pattern with (100), (002), (101), (102), (110), (103), (112) and (201) planes. The CNT peak was seen in the ZnO/CNT (0.1 wt%) pattern and improved with increasing CNT concentration until it was pronounce in the ZnO/CNT (0.5 wt%) sample. 41.93 and 41.03 nm were average crystallite size values calculated for as-synthesised ZnO and ZnO/CNT films respectively.

The optical properties of the as-synthesised ZnO varied with increasing concentration of CNT. The as-synthesised ZnO has bandgap of 3.488 eV as extrapolated from the bandgap plot. Bandgap energy values of 3.257, 3.152 and 3.013 eV were extrapolated for ZnO/CNT (0.1, 0.3 and 0.5 wt%) respectively. The optical transmittance spectra showed 83 %, 79 %, 73 % and 61 % characteristic optical transmittance for the as-synthesised ZnO and ZnO/CNT (0.1, 0.3 and 0.5 wt%) films respectively. This confirms the common saying amongst researchers that ZnO is a transparent conductive metal oxide material.

These results are evident that the structural and optical properties of the as-synthesised ZnO were enhanced with the introduction of CNT content.

5.2 Recommendation

It is recommended to get a new or sterilised Teflon lining be used for the hydrothermal autoclave in order to synthesise impurity free ZnO without contamination. It is also recommended to further characterise the as-synthesised samples using SEM, TEM in order to incorporate morphological features of the samples to the structural properties obtained. Also, it is recommended to fabricate a complete solar cell and carry out solar simulation so as to determine the power conversion efficiencies of the samples.

REFERENCES

Abdul, H., Sivaraj, R., and Venckatesh, R. (2014). Green Synthesis and Characterization of Zinc Oxide Nanoparticles from Ocimum Basilicum L. Var. Purpurascens Benth-Lamiaceae Leaf Extract. *Materials Letters,* 131 16–18.

Agnieszka, K. R., and Teofil, J. (2014). Zinc Oxide from Synthesis to Application: A Review. *Materials, 7*, 2833-2881.

Akhavan, O., Azimirad, R., and Safa, S. (2011). Functionalized Carbon Nanotubes in ZnO Thin Films for Photoinactivation of Bacteria. *Materials in Chemistry and Physics,* 130, 598–602.

Akhiruddin, S., and Irmansyah (2014). The Influence of Hydrothermal Duration on Structuresand Optical Properties of ZnO Nanoparticles. *Journal of Materials: Physics and Chemistry*, 2*, 34-3*6.

Alammar, T., and Mudring, A. V. (2009). Facile Ultrasound-Assisted Synthesis of Zno Nanorods in an Ionic Liquid. *Materials Letters, 63,* 732–735.

Ayesha N. U. H., Nadhman, A., Ullah, I., Mustafa, G., Yasinzai, M., and Khan, I. (2017). Synthesis Approaches of Zinc Oxide Nanoparticles: The Dilemma of Ecotoxicity. *Hindawi Journal of Nanomaterials*, 14, 8510342.

Ayeshamariam, A., Saravanakkumar, D., Kashif, M., Sivaranjani, S. and Ravikumar, B. (2016). Analysis on the effect of ZnO on Carbon Nanotube by Spray Pyrolysis Method. *Mechanics of Advanced Materials and Modern Processes*, 2(3), 1-8.

Baruwati, B., Kumar, D. K., and Manorama, S. V. (2006). Sensors Actuators B 119 676.

Bastiani, M. D. (2016). The Stability of Third generation solar cells, Ph.D thesis, Università degli Studi di Padova, Padova, Italy.

Bindu, P., and Sabu, T. (2014). Estimation of Lattice Strain in ZnO Nanoparticles: X-ray Peak Profile Analysis. *Journal for Theory of Applied Physics*, 8, 123–134.

Bréchignac, C., Houdy, P., and Lahmani, M. (2008). Nanomaterials and nanochemistry (Springer Science & Business Media).

Brintha, S.R., and Ajitha, M. (2015). Synthesis and Characterization of Zno Nanoparticles via AqueousSolution, Sol-Gel and Hydrothermal Methods. *IOSR Journal of Applied Chemistry*, 8 (11), 66-172.

Caglar, M., and Yakuphanoglu, F. (2012). Structural and Optical Properties of Copper Doped ZnO Films derived by Sol-gel. *Applied Surface Science*, 258, 3039-3044.

Cao, H. L., Qian, X. F., Gong, Q., Du, W. M., Ma, X. D., and Zhu, Z. K. (2006). Shape and Size-Controlled Synthesis of Nanometre ZnO from A Simple Solution Route at Room Temperature. *Nanotechnology, 17*, 3632–3636.

Chandu, V. V., Muralee, G., Seenu, R. S., Srinivasa, R., Araveeti, E. R, and Hee-Je, K. (2017). Carbon Nanotube/Metal-Sulfde Composite Fexible Electrodes for High-Performance Quantum Dot-Sensitized Solar Cells and Supercapacitors. *Scientific Reports*, 7, 46519.

Chang, J. H., and Lin, H. N. (2014). Investigation of the Photocatalytic Activity of ZnO Nanowires:Substrate Effect and Kinetics Analysis: *Journal of Nanomaterials*, 6.

Chapin, D. M., Fuller, C. S. and Pearson, G. L. (1954). A New Silicon p-n Junction Photocell for Converting Solar Radiation into Electrical Power, *Journal of Applied Physics,* 25, 676-677.

Cheng, B., and Samulski, E. T. (2004). Hydrothermal Synthesis of One dimensional ZnO Nanostructures with Different Aspect Ratios. *Chemical Communications,* 986–987.

Cheng, H. M., Chiu, W. H., Lee, C. H., Tsai, S. Y., and Hsieh, W.F. (2008). Formation of Branched ZnO Nanowires from Solvothermal Method and Dye-sensitized Solar Cells Applications: *Journal of Physical Chemistry C*, 112(42), 16359–16364.

Cullity, B. D. and Rstock, S. (2001). Elements of X-Ray Diffraction. Prentice Hall, New Jersey, NJ, USA, 2001.

Deepti, C., Simrjit, S., Vankar, V.D., and Neeraj, K. (2017). ZnO Nanoparticles Decorated Multi-Walled Carbon Nanotubes for Enhanced Photocatalytic and Photoelectrochemical Water Splitting. *Journal of Photochemistry and Photobiology,* 10, 1016.

Demianets, L. N., Kostomarov, D. V., Kuz’mina, I. P., and Pushko, S. V. (2002). Mechanism of Growth of ZnO Single Crystals from Hydrothermal Alkali Solutions. *Crystallography Reports,* 47(S1), S86–S98.

Dey, A., Bajpai, O.P., Sikder, A.K., Chattopadhyay, S., and Khan, M. A. S. (2016). Recent Advances in CNT/Graphene Based Thermoelectric Polymer Nanocomposite: a PAroficient move towards waste energy harvesting. *Renewable Sustaining Energy Revolution*, 53, 653-671

Díaz-Corona, N., Martínez-Juárez J., Pérez-Luna, J. G., Hernández-de, A. D., Luz, M., Rabana, E., and Robles-Águila, M. J. (2019). Structural, Optical and Electrical Behavior of ZnO/MWCNT Composite Thin Films. *Optical and Quantum Electronics*, 51 220-227.

Díaz-Corona, N., Martínez-Juárez, J., Pérez-Luna, J. G., Hernández-de, A. D., Luz, Rabanal, M. E. and Robles-Águila, M. J. (2019). Structural, Optical and Electrical Behavior of ZnO/ MWCNT Composite Thin Films. *Optical and Quantum Electronics*: 51:220.

Dibya, J. B. and Mostako, A. T. T. (2020). Investigation on Dispersion Parameters of Molybdenum Oxide Thin Films via Wemple–DiDomenico (WDD) Single Oscillator Model. *Applied Physics A,* 126, 818.

Djuriji, A. B., Chen X. Y., and Leung Y. H. (2012). Recent Progress in Hydrothermal Synthesis of Zinc Oxide Nanomaterials. *Recent Patents on Nanotechnology,* 6, 124-134.

Djurisic, A. B., Xi, Y. Y., Hsu, Y. F., and Chan, W. K. (2007). Hydrothermal Synthesis of Nanostructures. *Recent Patent on Nanotechnology*, 1, 121-128.

Du, Y., Hao, C., and Wang, G. (2008). Preparation of Floral-Patterned ZnO/MWCNT Heterogeneity Structure Using Microwave Irradiation Heating Method. *Materials Letters*, 62, 30–32.

Durgam, K., Eppa, R., Vijayakumar, Y., Sivakumar, J., Ramana R. M. V. and Sayanna, R. (2016). Optical, Structural and Morphological Properties of Photocatalytic ZnO Thin Films Deposited by Pray Pyrolysis Technique. *Modern Research in Catalysis*, 5, 130-146.

Dutta, M., and Basak, D. (2009). Multiwalled Carbon Nanotubes/Zno Nanowires Nanocomposite Structure with Enhanced Ultraviolet Emission and Faster Ultraviolet Response. *Chemical Physics Letters*, 480, 253-257.

Eman, A., Mwafya, M., Dawya, A., Abouelsayedb, I., Elsabbaghc A., and Elfass, M. M. (2016). Synthesis and Characterization of Multi-Walled Carbon Nanotubes Decorated ZnO Nanocomposite. *Egyptian Journal of Chemistry,* 59(6), 1061– 1068.

Ezenwa, I.A. (2012). Synthesis and Optical Characterization of Zinc Oxide Thin Film. *Research Journal of Chemical Sciences*; 9, 26–30.

Fang, B., Zhang, C., Zhang, W., and Wang, G. (2009). A Novel Hydrazine Electrochemical Sensor Based on a Carbon Nanotube-wired ZnO Nanoflower-modified Electrode. *Electrochemica Acta,* 55, 178-182.

Fang, L., Jui-Fu, Y., and Shou-Yi, K. (2015). Efficiency Enhancement of Dye-Sensitized Solar Cells' Performance with ZnO Nanorods Grown by Low-Temperature Hydrothermal Reaction. *Materials, 8*, 8860–8867.

Gadallah, A. S., and El-Nahass, M. M. (2013). Structural, Optical Constants and Photoluminescence of ZnO Thin Films Grown by Sol-Gel Spin Coating. *Advances in Condensed Matter Physics*, 234546, 11.

Gertner, J. (2013). *The Idea Factory: Bell Labs and the Great Age of American Innovation*: Penguin Books.

Goldstein, J. I., (2003). Scanning Electron Microscopy and X-ray Micronalysis, 3rd ed, Plenum Press, New York.

Gratzel, M. (2001). Photoelectrochemical Cells. *Nature,* 414, 338-344.

Green, M. A. (2006). Third Generation Photovoltaics. Springer.

Green, M. A., Ho-Baillie, A. and Snaith, H. J. (2014). The Emergence of Perovskite Solar Cells, *Nature Photonics,* 8, 506–514.

Guadalupe, G. V., Jesús, V. S. J., José, E. S. B., Hiram, J. O. G., Josefina, A. J. M., Karí, G. H. M. R., Miguel, J. Y., Hugo, R. N. C. (2018). Zinc Oxide Decorated Multiwalled Carbon Nanotubes: Their BolometricProperties.*Nanotechnology*, 91, 1361-6528.

Guler, Ö., Guler, S. H., Yo, F., Aydin, H., Aydin, C., El-Tantawy, F., Duraia, E. M., Fouda, A. N., (2015). Electrical and Optical Properties of Carbon Nanotube Hybrid Zinc Oxide Nanocomposites Prepared by Ball Mill Technique. *Fullerenes, Nanotubes and Carbon Nanostructures,* 10 (256), 1-23.

Gültekin, D., Alaf M. and Akbulut, H. (2013). Synthesis and Characterization of ZnO Nanopowders and ZnO-CNT Nanocomposites Prepared by Chemical Precipitation Route. *Acta Physica Polonica A,* 123 (2), 274-278.

Happy, A., Kumar, S. V., and Rajeshkumar, S. (2017). A Review on Green Synthesis of Zinc Oxide Nanoparticles: An Eco-friendly Approach. *Resource-Efficient Technologies,* 3, 406–413.

Haruna I., Muhammad M. K., Abubakar S., Mohammed I. K. And Kasim U. I. (2019); Review on Hydrothermal Synthesis of ZnO; *Second School of Sciences Biennual International Conference (SPSBIC). Theme: Sustainable Energy in Changing Climate*. *The Role of Science and Technology,* 2.

Hiromichi, H., and Yukiya, H. (2010). Review: Hydrothermal Synthesis of Metal Oxide Nanoparticles in Supercritical Water. *Open Access Materials,* 3, 3794-3817.

Hofmann, P. (2008). Solid State Physics: Wiley-VCH.

Hoshino, A., Fujioka, K., and Oku, T. (2004). Quantum Dots Targeted to the Assigned Organelle in Living Cells. *Microbiology and Immunology,* 48(12), 985–994.

Hossain, S., Quaderi, G. D. A., Hussain, K. M. A. and Faruqe, T. (2018). Synthesis and Characterization of Undoped and Aluminum Doped Zinc Oxide Thin Films using Thermal Evaporation Method. *Nuclear Science and Applications*: 27 (12), 25.

Jackson, P., Hariskos D., Lotter E., Paetel S., WUERT R., Menner R., Wischmann, W., and Powalla, M. (2011). New World Record Efficiency for Cu(In,Ga)Se_2 Thin-film Solar Cells beyond 20%, *Progress in Photovoltaics: Research and Applications,* 19 (7), 894-897.

Janotti, A., and Walle, C. G. V. D. (2011). Fundamentals of Zinc Oxide as a Semiconductor. *Rep. Prog. Phys.*72 (126501) 29.

Jezequel, D., Guuenota, J., Jouinia, N., and Fievet, F. (2010). Submicronic Zinc Oxide Particles: Elaboration in Poly Medium and Morphological Characteristics. *Journal of Materials Res*earch, 12, 77-83.

Jiaguo, Y., and Xiaoxiao, Y. (2008). Hydrothermal Synthesis and Photocatalytic Activity of Zinc Oxide Hollow Spheres. *Environmental Science. Technology,* 42, 4902–4907.

Karuna, P. G., Shweta, N. J., and Rohidas, B. K. (2018). Influence of pH on Hydrothermally Derived Zno Nanostructures. *Elsevier Optik,* 156, 758–771.

Kasim Uthman Isah (2013). Optical and Morphological Studies of Chemical Bath Deposited Nanocrystalline Cd_{1-x} Zn_x S Thin Films. *Materials Sciences and Applications,* 4, 287-292.

Kawska, A., Duchstein, P., Hochrein, O., and Zahn, D. (2008). Atomistic Mechanisms of Zno Aggregation from Ethanolic Solution: Ion Association, Proton Transfer, and Self-Organization. *NanoLetters,* 8, 2336–2340.

Klanwan, J., Akrapattangkul, N., Pavarajarn, V., Seto, T., Otani, Y., and Charinpanitkul, T. (2010). Single-step Synthesis of MWCNT/ZnO Nanocomposite Using Co-chemical Vapor Deposition Method. *Materials Letters*, 64, 80–82.

Ko, S. H., Lee, D., and Kang, H. W. (2011). Nanoforest of Hydrothermally Grown Hierarchical ZnO Nanowires for A High Efficiency Dye-sensitized Solar cell. *Nano Letters*, 11(2), 666–671.

Lai, W. C., Chen, J.T., and Yang, Y.Y., (2013). ZnO-SiO2 Solar-blind Photodetectors on Flexible Polyethersulfone Substrate with Organosilicon Buffer Layer. *Applied Physics Letters*, 102 (19), 111-115.

Larry, D., and Hanke, P.E (2010): Handbook of Analytical Methods for Materials Practical Solutions to Materials Problems: Through Technology and Innovation. *Materials Evaluation and Engineering, Inc.*

Laurent, S., Anne C., Patrick, L., Daniel, G., and Geneviève, P. (2015). Optimization of a New ZnO Nanorods Hydrothermal Synthesis Method for Solid State Dye Sensitized Solar Cells Applications.

Lawrence, C., Feng, J., Owen, A., and Pawar S. (2013). Synthesis of Zinc Oxide Nanomaterials via Solution Synthesis Method. *Journal of Nanomaterials*, *15*, 312-315.

Lee, J. J., Lee, S. H., Kim, F. S., Choi, H. H., and Kim, J. H. (2015). Simultaneous Enhancement of the Efficiency and Stability of Organic Solar Cells using Pedot: PSS Grafted with a Pegme Buffer Layer. *Organisation of Electronics*, 26, 191-199.

Lee, J., Sorescu, C. D., and Deng, X. (2018). Tunable Lattice Constant and Band Gap of Single and Few-Layer ZnO. *National Energy Technology Laboratory*, *U. S. Department of Energy*, 152 (36) 1-21.

Lee, K., Lai, C. W., Ngai, K. S., and Juan, J. C. (2016). Recent Developments of Zinc Oxide Based Photocatalyst in Water Treatment Technology: A review. *Water Resources*, 88, 428–448.

Liu J., Li, X., and Dai, L. (2006). Water Assisted Growth f Aligned Carbon Nanotube-Zno Heterojunction Arrays. *Advanced Materials Research,* 18, 1740-1744.

Liu, B., and Zeng, H. C. (2003). Hydrothermal Synthesis of Zno Nanorods in the Diameter Regime of 50 nm; *Journal of American Chemical Society*, *125*, 4430–4431.

Lu, C. H., and Yeh, C. H. (2000). *Ceramics Integration*, 26, 35.

Luo, G., Ren, X., Zhang, S., Wu, H., Choy, W. C. H., He, Z., and Cao, Y. (2016). Recent Advances in Organic Photovoltaics: Device Structure and Optical Engineering Optimization on the Nanoscale. *Small* ,12, 1547-1571.

Lupan, O. Guerin, V. M. and Tiginyanu, I. M. (2010). Well-aligned Arrays of Vertically Oriented ZnO Nanowires Electrodeposited on ITO-coated Glass and their Integration in Dye-sensitized Solar Cells. *Journal of Photochemistry and Photobiology A*, 211, (1), 65–73.

Luque, S. H. (2003). *Handbook of Photovoltaic Science and Engineering,* Wiley-VCH.

Mansour, S. A., and Yakuphanoglu, F., (2012). Electrical-Optical Properties of Nano-Fiber ZnO Film Grown by Sol-gel Method and Fabrication of ZnO/p-Si Heterojunction. *Solid State Sciences*, 14, 121-126.

Mei, W., Lin, M., Chen, C., Yan, Y., and Lin, L. (2018). Low-temperature Synthesis and Sunlight-catalytic Performance of Flower-like Hierarchical Graphene Oxide/ZnO Macrosphere. *Journal of Nanoparticle Research,* 286, 297.

Miller, O. D., Yablonovitch, E. and Kurtz, S. R. (2012). Strong Internal and External Luminescence as Solar Cells Approach the Shockley Queisser Limit. *Photovoltaics, IEEE Journal of Photovoltaics,* 2, 303-311.

Min, Y.L., *et al*., (2011). Field Emission Property of Printed CNTs-Mixed ZnO Nanoneedles; *Applied Surface Science,* 257, 6332-6335.

Mohamed, S.H. (2012). Synthesis, Structural and Elliposmetric Evaluation of Oxygen-deficient and Nearly Stiochiometric Zinc Oxide and Indium Oxide Nanowire/nanoparticles; *Philosophical Magazine*; 3598–3612.

Mohammaznezhad, M., Selopal, G. S., Wang, Z. W., Stansfield, B., Zhao, H., and Rosei, F. (2018). Thermal Stability of Dye Sensitized Solar Cells Using Multi Walled Carbon Nanotubes: *A Genuinely Multidisciplinary Chemical Journal Centering on Chemistry*.

Morusu, M. (2012). Investigation of CZTSe Solar Cell with ZnS, ZnSe and In2S3as Buffer Layers, M.Sc thesis, The University of Toledo.

Nelson, J. (2003). The Physics of Solar Cells. London: Imperial College Press, 363.

Nessa, F. S. (2013). Structural, Electrical and Optical Properties of Transparent Conducting Si-doped ZnO Thin Films Grown by Pulsed Laser Deposition. University of Birmingham Research Archive e-theses repository.

Ong, B.C., Ng, Y. L., and Mohammad, W.A. (2018). A Review of ZnO Nanoparticles as Solar Photocatalysts: Synthesis, Mechanisms and Applications. *Renewable and Sustainable Energy Reviews,* 81, 536–551.

Oriaku, C. I., and Osuwa, J. C. (2009). On the Optical Dispersion Parameters of Thin Film Al^{3+} Doped ZnO Transparent Conducting Glasses. *Journal of Ovonic Research,* 5(6), 213-218.

Petkova, P., Nedelchev, L., Nazarova, D., Boubaker, K., Mimouni, R., Vasilev, P., Alexieva, G. and Bachvarova, D. (2017). Single oscillator model of undoped and co-doped ZnO thin films. *Optik*, 139, 217–221.

Prajapati, C. S., Kushwaha, A., and Sahay, P. P. (2013). “Experimental Investigation of Spray-Deposited Fe-doped ZnO Nanoparticle Thin Films: Structural, Microstructural, and Optical Properties. *Journal of Thermal Spray Technology*, 22 (7), 1230–1241.

Prayut, P., Chokchai, K., and Wisanu, P. (2010). Synthesis and Characterization of Carbon Nanotube/Zinc Oxide Composites.

Prayut, P., Wisanu, P., and Wichan, T. (2014). Microwave Assisted Synthesis of ZnO/MWCNT Hybrid Nanocomposites and their Alcohol-sensing Properties. *Journal of Experimental Nanoscience,* 9(1), 96-105.

Rasin, A. T. (2014). High Efficiency Quantum Dot-sensitised Solar Cells by Material Science and Device Architecture, Ph.D Thesis, Queensland University of Technology, Brisbane, Australia.

Rayees, A. Z, Manju, A., Alshahrani, T., and Shkir, M. (2020). Screen Printed Novel ZnO/MWCNTs Nanocomposite Thick Films. *Ceramics International*, 10, 85.

Richard, C. B., Charles A. E., and Wilson, Jr. S. (1992). Encyclopedia of Materials Characterization. 146, 70-74.

Rika, N. S., Suriani, A. B., Suhufa, A., Azmi, M., Norhayati, H., Azlan, K., Illyas, M. I., Mohamad, R. M., and Abdul, R. M. (2015). Zinc Oxide/Carbon Nanotubes Nanocomposite: Synthesis Methods and Potential Applications. *Advanced Materials Research*, 1109, 45-49.

Septiani, N. L. W., Yuliarto, B. Nugraha, and Dipojono, H. K. (2017). Multiwalled Carbon Nanotubes-zinc Oxide Nanocomposites as Low Temperature Toluene Gas Sensor. *Applied Physics Article,* 123, 166.

Serbetçi, Z., El-Nasser, H. M., and Yakuphanoglu, F., (2012). Photoluminescence and Refractive Index Dispersion Properties of ZnO Nanofibers Grown by Sol-gel Method. *Spectrochimica Acta Part A,* 86, 405-409.

Shanmuganathan, G., and Shameem B. I. B., (2014). Influence of Codoping on the Optical Properties of ZnO Thin Films Synthesized on Glass Substrate by Chemical Bath Deposition Method. *Advances in Condensed Matter Physics*, 761960, 9.

Sheng, X., and Zhong L. W. (2014). One-Dimensional ZnO Nanostructures: Solution Growth and Functional Properties. *Nano Research*, 7, 011-0160.

Shkir, M., Al-Shehri, B.M., Pachamuthu, M., Khan, A., Chandekar, K.V., AlFaify, S., Hamdy, M.S. (2020). A Remarkable Improvement in Photocatalytic Activity of ZnO Nanoparticles through Sr Doping Synthesized by One Pot Flash Combustion Technique for Water Treatments, Colloids and Surfaces A: *Physicochemical and Engineering Aspects* 587 124340.

Shockley, W. and Queisser, H. (1961). Detailed Balance Limit of Efficiency of p-n Junction Solar Cells, *Journal of Applied Physics*, 32, 510-519.

Shu, Z., Xin, L., Weihua, L., Yongning, H., Zhihao, X., and Changchun, Z. (2010). Field Emission Properties of the Dendritic Carbon Nanotubes Film Embedded with ZnO Quantum Dots. *Journal of Nanomaterials,* 5, 45.

Singh, R., Bhushan, S., Singh, A., Deo, S. (2011). Characterization and Optical Properties of CdSe Nanocrystalline Thin Films. *Digest Journal of Nanomaterials and Biostructures*, 6(2), 403.

Streetman, B. and Banerjee, S. (2005). Solid State Electronic Devices: Prentice Hall.

Subodh, K. (2006). Organic Chemistry: Spectroscopy of Organic Compounds.

Sudhagar, P., Kumar, R. S.,and Jung J. H. (2011). Facile Synthesis of Highly Branched Jacks-like ZnO Nanorods and their Applications in Dye-sensitized Solar Cells: *Materials Research Bulletin*, 46(9), 1473–1479.

Sui, M., Zhang, L., Sheng, L., Huang, S., and She, L. (2013). Synthesis of ZnO Coated Multi-walled Carbon Nanotubes and their Antibacterial Activities. *Science of the Total Environment,* 452, 148–154.

Sunandan, B., and Joydeep, D. (2009). Topical Review: Hydrothermal Growth Of Zno Nanostructures. *Science and Technology Advanced Materials,* 10, 18.

Wang, H.Y., and Chua, D.H.C. (2012). Triple Layered Core-Shell Structure with Surface Fluorinated ZnO Carbon Nanotube Nanocomposites and Its Electron Emission Properties; *Applied Surface Science,* 265, 66-70.

Wang, X., Xia, B., Zhu, X., Chen, J., Qiu, S., and Li, J. (2008). Controlled Modification of Multiwalled Carbon Nanotubes with Zno Nanostructures. *Journal of Solid State Chemistry,*181, 822–827.

Wayu, M. B., Spidle, R. T., Devkota, T., Deb, A. K., Delong, R. K., Ghosh, K. C., Wanekaya, A. K., Chusuei, C. C. (2013). Morphology of Hydrothermally Synthesized ZnO Nanoparticles Tethered to Carbon Nanotubes Affects Electrocatalytic Activity for H_2O_2Detection. *Electrochimica Acta*, 97, 99–104.

Wei-Chen, C., Yao-Yi, C., Wan-Chin, Y., Yih-Chun, Y., Chia-Hua, L. and Hung-Han, K. (2012). Enhancing Performance of ZnO Dye-sensitized Solar Cells by Incorporation of Multiwalled Carbon Nanotubes. *Nanoscale Research Letters*, 7 (166), 1-7.

Whitesides, G. M., Kriebel, J. K., and Mayers, T. B. (2005). Nanoscale Assembly Chemical Techniques 217 (Springer).

Xia, Y., Yang, P., and Sun Y. (2003). One-dimensional Nanostructures: Synthesis, Characterization, and Applications. *Advanced Materials,* 5, 353–389.

Xolani, G., Mbuyise, E. A. A., Arbab, K., Kaviyarasu, G., Pellicane, M., and Maaza, G. T. M. (2017). Zinc Oxide Doped Single Wall Carbon Nanotubes in Hole Transport Buffer Layer. *Journal of Alloys and Compounds,* 706, 344-350.

Xu, S., Lao, C., Weintraub, B., and Wang, Z. L. (2008). Density Controlled Growth of Aligned ZnO Nanowire Arrays by Seedless Chemical Approach on Smooth Surfaces. *Journal of Materials Research,* 8, 2072–2077.

Yangyang, Z., Ram, M. K., Stefanakos, E. K., and Goswami, D. Y. (2012). Review Article: Synthesis, Characterization, and Applications of ZnO Nanowires. *Journal of Nanomaterials,* 22, 2012.

Yipeng, D., Chun, C, H., and Guizhen, W. (2008). Preparation of Floral-Patterned ZnO/MWCNT Heterogeneity Structure Using Microwave Irradiation Heating Method. *Materials Letters*, 62, 30–32.

Zhang, J., Sun, L. D., Yin, J. L., Su, H. L., Liao, C. S., and Yan, C. H. (2002). Control of ZnO Morphology via a Simple Solution Route. *Chemical Materials*, 14, 4172–4177.

Zhang, Q., Dandeneau, S. C., Zhou, X., and Cao, G. (2009). ZnO Nanostructures for Dye Sensitized Solar Cells. *Advanced Materials*, 21, 4087–4108.

Zhang, Y., *et al*. (2009). Carbon Nanotube/Zinc Oxide Electrode and Gel Polymer Electrolyte for Electrochemical Supercapacitors. *Journal of Alloys Compounds*, 480, 17-19.

Zhang, Y., Ram, M. K., Stefanakos, E. K., and Goswami, D. Y. (2012). Review Article: Synthesis, Characterization, and Applications of ZnO Nanowires. *Journal of Nanomaterials*, 22, 624520.